Research Square

Preprints are preliminary reports that have not undergone peer review.
They should not be considered conclusive, used to inform clinical practice,
or referenced by the media as validated information.

Distinct GPER ligands engage divergent RIPK1 regulatory states linked to necroptotic cell death

Jung-Ae Kim

jakim@yu.ac.kr

Yeungnam University https://orcid.org/0000-0002-0824-8532

Kiran Yadav

YeungnamUniversity

Kalpana Ghimire

Yeungnam University

Hee Dong Park

Innovo Therapeutics Inc

Dongchul Lim

Innovo Therapeutics Inc

Byeong- Seon Jeong

Article

Keywords: G protein-coupled estrogen receptor (GPER), Receptor-interacting protein kinase 1 (RIPK1), Ubiquitin remodeling, Molecular Docking, G1, BJ-2136

Posted Date: November 23rd, 2026

DOI: https://doi.org/10.21203/rs.3.rs-9890932/v1

License: This work is licensed under a Creative Commons Attribution 4.0 International License.
Read Full License

Additional Declarations: There is no conflict of interest

Distinct GPER ligands engage divergent RIPK1 regulatory states linked to necroptotic cell death

Kiran Yadav[1], Kalpana Ghimire[1], Hee Dong Park[2], Dongchul Lim[2,*], Byeong-Seon Jeong[1,*], Jung-Ae Kim[1,*]

[1]*College of Pharmacy, Yeungnam University, Gyeongsan 38541, Republic of Korea*

[2]*Innovo Therapeutics Inc., Daeduck biz center C-313, 17 Techno 4-ro, Yuseong-gu, Daejeon 34013, Republic of Korea*

Running title: GPER ligands and RIPK1-dependent necroptosis

*__Corresponding authors:__ J-A Kim (jakim@yu.ac.kr), D Lim (dclim@innovothera.com) and B-S Jeong (jeongb@ynu.ac.kr)

Jung-Ae Kim, Ph.D., College of Pharmacy, Yeungnam University, Gyeongsan 38541, Republic of Korea; Phone: +82-53-810-2816; Fax: +82-53-810-4654.

Dongchul Lim, Ph.D. Innovo Therapeutics Inc., Daeduck biz center C-313, 17 Techno 4-ro, Yuseong-gu, Daejeon 34013, Republic of Korea; Phone: +82-42-721-0012; Fax: +82-42-721-0073.

Byeong-Seon Jeong, Ph.D., College of Pharmacy, Yeungnam University, Gyeongsan 38541, Republic of Korea; Phone: +82-53-810-2814; Fax: +82-53-810-4654.

ABSTRACT

G protein-coupled estrogen receptor (GPER) regulates diverse cellular responses, but its involvement in receptor-interacting protein kinase 1 (RIPK1)-dependent cell death remains poorly understood. We investigated how pharmacologically distinct GPER ligands affect RIPK1 regulation and cell fate. GPER co-immunoprecipitated with RIPK1, and modulation of GPER expression altered RIPK1 protein abundance without corresponding changes in RIPK1 mRNA. The GPER agonist G1 and antagonist G15 increased RIPK1–RIPK3–MLKL phosphorylation and induced RIPK1-dependent cell death, whereas the structurally distinct agonist BJ-2136 stimulated cAMP production without comparable RIPK signaling or cytotoxicity. G1 enhanced the recovery of RIPK1, RIPK3, and MLKL in GPER immunoprecipitates, whereas G15 activated the RIPK3–MLKL pathway without detectable co-recovery with GPER under the conditions examined. Both G1 and G15 increased K48-linked and decreased K63-linked RIPK1 ubiquitination, and these changes persisted after GPER depletion. Both ligands also enhanced total RIPK1 ubiquitination in a GPER-free reconstituted system, indicating a GPER-independent component of their effects. Necrostatin-1 attenuated RIPK3/MLKL phosphorylation, endoplasmic reticulum stress, and cell death, whereas caspase inhibition had little effect. G1 and BJ-2136 showed GPER-dependent calcium mobilization, supporting functional receptor engagement, while molecular docking predicted partially overlapping binding poses with distinct ligand interactions within the GPER binding cavity. Together, these findings reveal distinct GPER-associated signaling and GPER-independent regulation of RIPK1 ubiquitination, highlighting the divergence between GPER-mediated signaling and RIPK1-dependent necroptotic cell death.

Keywords: G protein-coupled estrogen receptor (GPER); Receptor-interacting protein kinase 1 (RIPK1); Ubiquitin remodeling; Molecular Docking; G1; BJ-2136

INTRODUCTION

Regulated cell death and survival signaling are tightly coordinated processes that determine cancer cell fate and therapeutic response [1]. Among non-apoptotic death programs, necroptosis has emerged as a critical caspase-independent cell death program that can operate when apoptotic signaling is compromised. This pathway is mediated by the receptor-interacting protein kinases RIPK1 and RIPK3, together with the executioner protein MLKL, and promotes antitumor immunity through the release of immunogenic danger signals [2, 3]. Conversely, cancer cells engage multiple growth and survival pathways, including Ras–Raf–MAPK and PI3K–Akt signaling, to withstand cellular stress and death-inducing stimuli [4, 5]. At the intersection of these opposing responses, RIPK1 functions as a context-dependent signaling checkpoint that integrates extracellular signals to determine cell fate. Depending on its kinase activity, ubiquitination status, and interactions with adaptor proteins, RIPK1 can support cell survival via NF-κB and MAPK signaling or alternatively initiate apoptosis and necroptosis [6, 7]. This functional plasticity has positioned RIPK1 as a pivotal regulator of inflammation, oncogenesis, and therapy response, driving substantial interest in its pharmacological modulation in cancer [2, 8]. Despite this progress, the upstream receptor systems that bias RIPK1 signaling toward survival or necroptotic cell death in cancer cells remain incompletely defined.

The G protein-coupled estrogen receptor (GPER, also termed GPER1 or GPR30) is a non-classical estrogen receptor implicated in diverse aspects of cancer biology, including proliferation, migration, metabolism, and therapeutic responsiveness across multiple tumor types [9, 10]. Although GPER has been predominantly studied as a mediator of rapid estrogen-dependent growth and survival signaling, accumulating evidence indicates that its functional repertoire extends to stress-responsive and cell death pathways. Notably, genetic deletion of GPER was recently shown to suppress triple-negative breast cancer cell growth through activation of the JNK/c-Jun/p53/Noxa signaling cascade, implicating GPER as an upstream regulator of stress-

responsive apoptotic signaling [11]. These observations broaden the functional scope of GPER beyond conventional estrogen-responsive signaling and raise an important question as to whether GPER may also interface with non-apoptotic cell death machinery.

Pharmacological interrogation of GPER has relied predominantly on the synthetic ligands G1, a highly selective agonist, and G15, a structurally related antagonist [12, 13]. These compounds have been widely used to delineate GPER function in cancer and neurological injury models, with G1 generally recapitulating estrogenic GPER signaling and G15 antagonizing GPER-dependent responses [14, 15]. However, the structural basis of ligand recognition and activity at GPER remains incompletely defined. While early interpretations relied largely on homology models, recent GPER–Gq cryo-electron microscopy structures have provided an experimental framework for investigating ligand–receptor interactions [16, 17]. Notably, the Lys05-bound structure (PDB 8XOF) identified a ligand-occupied binding cavity, whereas structures obtained with conventional GPER ligands, including G1, did not resolve corresponding ligand densities. These observations leave open the possibility that structurally distinct GPER ligands engage different binding interactions, potentially contributing to divergent pharmacological responses. This possibility is particularly relevant to cell death signaling, as our previous study reported GPER-independent necroptotic effects of G1 and G15 [18], revealing an unexpected functional connection between GPER pharmacology and RIPK1-dependent cell death.

Whether G1 and G15 merely exert opposing pharmacological effects at GPER or instead produce distinct regulatory effects on RIPK1 and cell fate remains unresolved. In particular, it is unknown how pharmacologically distinct GPER ligands influence RIPK1 abundance and stability, receptor-associated signaling complex organization, and the ubiquitin modifications that critically govern RIPK1 function. Moreover, whether these regulatory events converge on RIPK1–RIPK3–MLKL signaling to influence necroptotic versus survival outcomes has not been established. This question is further underscored by the development of structurally distinct GPER-targeting

compounds, including BJ-2136, a substituted benzothiophene–trimethylpyridinol scaffold with agonistic activity at GPER [18]. The availability of these ligands provides an opportunity to investigate the relationship between GPER-associated signaling, RIPK1 regulation, and cell death while examining whether distinct pharmacological responses are accompanied by differences in predicted ligand–receptor interactions.

In this study, we investigated how pharmacologically distinct GPER ligands influence RIPK1 regulation and downstream cell death signaling. Using genetic, pharmacological, and biochemical approaches, we examined the effects of G1, G15, and BJ-2136 on RIPK1 abundance and stability, receptor-associated complex organization, ubiquitination, and RIPK1–RIPK3–MLKL signaling. To complement these functional analyses, we compared the Ca^{2+}-mobilizing activities of BJ-2136 and G1 and examined their responses to GPER modulation and G15 antagonism. We further employed structure-guided docking and interaction profiling to explore the predicted binding of BJ-2136 and G1 within the experimentally identified GPER ligand-binding cavity, including comparisons with water positions observed in the apo-GPER structure. These computational analyses were intended to generate hypotheses regarding ligand–receptor interactions rather than establish experimentally validated binding modes. Together, these approaches were designed to clarify the relationship between GPER pharmacology, RIPK1 regulatory states, and RIPK1-dependent cell death.

RESULTS

Basal RIPK1 abundance and phosphorylation are associated with GPER expression

Across cancer and non-cancer cell lines, higher basal GPER abundance was generally associated with increased RIPK1 protein and phosphorylation (Fig. 1A). Consistent with this relationship, GPER overexpression in COS-7 cells increased RIPK1 abundance and basal phosphorylation,

whereas GPER knockdown in COS-7-GPER^{OV} cells reduced RIPK1 protein levels and RIPK3 phosphorylation (Fig. 1A, B). Despite these protein-level changes, RIPK1 mRNA remained largely unchanged following GPER manipulation (Fig. 1C), suggesting post-transcriptional regulation.

Cycloheximide (CHX), an inhibitor of new protein synthesis, was used to assess GPER and RIPK1 persistence in matched cellular backgrounds. RIPK1 showed greater relative persistence than GPER in GPER-overexpressing COS-7 (COS-7-GPER^{OV}) and control PC-3 cells, whereas their decay profiles were similar in parental COS-7 and GPER-depleted PC-3 cells (Fig. 1D). However, these comparisons did not establish a statistically significant difference in RIPK1 half-life between GPER-high and GPER-low conditions.

We next tested whether GPER abundance influenced sensitivity to G1, G15, and BJ-2136. G1 and G15 reduced viability in both COS-7 and PC-3 cellular models, whereas BJ-2136 exhibited minimal cytotoxicity. Notably, COS-7-GPER^{OV} cells were less sensitive to G1 than parental cells, and GPER depletion did not abolish G1- or G15-induced cytotoxicity in PC-3 cells. In contrast, RIPK1 knockdown attenuated the cytotoxic effects of both ligands across the cellular backgrounds examined (Fig. 1E). G1 and G15 induced cellular swelling, membrane disruption, and increased propidium iodide uptake, unlike BJ-2136 (Fig. 1F). Together, these results indicate that ligand-induced cytotoxicity is more closely associated with RIPK1 dependence than with cellular GPER abundance.

Ligand-specific RIPK1 phosphorylation and cytotoxicity are uncoupled from transcriptional responses

We next compared RIPK1 responses to G1 and G15 with those elicited by the GPER agonists BJ-2136 and CITFA and the antagonist CIMBA (Fig. 2A). G1 and G15 markedly reduced PC-3 cell viability and increased RIPK1 phosphorylation, whereas BJ-2136, CITFA, and CIMBA showed

minimal cytotoxicity or p-RIPK1 induction (Fig. 2B, C). In contrast, GPER protein abundance increased following treatment with G1, BJ-2136, or CITFA, without a corresponding relationship to RIPK1 phosphorylation or cytotoxicity.

We next assessed whether transcription explained these differences. G1 enhanced the time-dependent GPER mRNA response, whereas G15 and BJ-2136 had no significant overall effect. G1 and G15 transiently increased RIPK1 mRNA by approximately twofold, while BJ-2136 had little effect (Fig. 2D, E). Actinomycin D suppressed both transcripts regardless of ligand treatment.

Basal RIPK1 abundance varied over time in vehicle-treated cells (Fig. 2F). At the protein level, G1 and BJ-2136 increased GPER protein, whereas G15 did not. In contrast, G1 and G15 progressively increased RIPK1 phosphorylation without sustained accumulation of total RIPK1, while BJ-2136 had little effect on either parameter (Fig. 2G). Under cycloheximide-mediated translational blockade, GPER, RIPK1, and p-RIPK1 declined, with no ligand sustaining total RIPK1 abundance (Fig. 2G). Thus, G1- and G15-induced RIPK1 phosphorylation was disproportionate to changes in RIPK1 mRNA or protein.

Distinct GPER ligands engage divergent RIPK1 signaling architectures

To explore a potential contribution of proteasomal turnover to RIPK1 regulation, we examined proteasomal inhibition with MG-132. This treatment increased the abundance of GPER, RIPK1, and phosphorylated RIPK1 (p-RIPK1) in PC-3 cells (Fig. 3A). G1 and BJ-2136 also increased GPER abundance, with further accumulation upon MG-132 co-treatment, whereas G15 had little effect alone. In contrast, G1 and G15 markedly enhanced RIPK1 phosphorylation without increasing total RIPK1, and MG-132 further augmented this response. BJ-2136 did not appreciably alter RIPK1 phosphorylation.

To determine whether ligand-dependent RIPK1 regulation is accompanied by changes in its association with GPER, we performed co-immunoprecipitation assays. Basal GPER–RIPK1 association was detected in both PC-3 and COS-7-GPER^{OV} cells (Fig. 3B, C). G1 increased GPER recovery in RIPK1 immunoprecipitates alongside increased input GPER, whereas BJ-2136 increased input GPER without a comparable increase in co-recovery. Despite similar RIPK1 immunoprecipitation and associated p-RIPK1, G1 and G15, but not BJ-2136, increased RIPK1-associated p-RIPK3. In contrast, BJ-2136 robustly increased intracellular cAMP, whereas G1 elicited only a minimal response and G15 and CIMBA had no detectable effect (Fig. 3D). G15 and CIMBA suppressed BJ-2136-induced, but not forskolin-stimulated, cAMP production.

GPER depletion did not abolish G1- or G15-induced RIPK3 and MLKL phosphorylation (Fig. 3E). Both ligands also increased Annexin V$^+$/PI$^+$ cell populations over time (Fig. 3F) and induced the ER stress markers BiP and CHOP (Fig. 3G), whereas BJ-2136 produced minimal Annexin V$^+$/PI$^+$ staining.

To distinguish ligand-specific complex recruitment from pathway activation, we compared TNF-α responses (Fig. 3H). In whole-cell lysates (input), TNF-α, G1, and G15 increased RIPK1, RIPK3, and MLKL phosphorylation. p-FADD increased prominently following TNF-α stimulation, and G1, unlike G15, attenuated this TNF-α-induced increase during co-treatment. In GPER immunoprecipitates, TNF-α alone produced only trace recovery of RIPK1, RIPK3, and MLKL, whereas G1 markedly increased their association with GPER, including phosphorylated RIPK1, RIPK3, and MLKL. In contrast to the input response, total FADD was detected in GPER immunoprecipitates at levels comparable between vehicle- and G1-treated cells, without a G1-dependent increase in co-immunoprecipitated p-FADD; caspase-8 was not appreciably co-recovered. TNF-α co-treatment reduced GPER-associated phosphorylated RIPK proteins despite pathway activation in whole-cell lysates. In contrast, G15 activated RIPK1–RIPK3–MLKL

signaling without detectable association of these proteins with GPER, distinguishing its signaling organization from that observed with G1.

Finally, we examined whether 17β-estradiol (E2), an endogenous estrogen, elicited comparable RIPK1 signaling. E2 increased GPER abundance and transiently elevated RIPK1 phosphorylation at 1–4 h, without significant activation of RIPK3 or MLKL or detectable FADD phosphorylation and caspase-8 activation (Fig. 3I). Thus, E2-associated RIPK1 phosphorylation did not progress to downstream necroptotic signaling.

GPER ligands differentially remodel GPER- and RIPK1-associated ubiquitination

We next compared GPER and RIPK1 ubiquitination, which can regulate receptor trafficking and death signaling (Fig. 4A–C). G1 transiently increased ubiquitination of both proteins, whereas BJ-2136 preferentially enhanced GPER ubiquitination and G15 predominantly increased RIPK1 ubiquitination. G1- and BJ-2136-induced GPER ubiquitination was accompanied by altered cell-surface GPER antibody accessibility, a response not observed with G15 (Fig. 4D).

Linkage-specific analysis of GPER immunoprecipitates showed basal K48-linked ubiquitination that decreased with G1, BJ-2136, or G15 (Fig. 4E). In contrast, basal K63-linked ubiquitination was low but increased in response to G1 and BJ-2136, with no appreciable change following G15 treatment (Fig. 4F). Thus, G1 and BJ-2136 altered GPER ubiquitination, whereas G15 preferentially affected RIPK1.

Ligand-specific remodeling of RIPK1 ubiquitination and its relationship to GPER abundance and necroptotic signaling

We next examined RIPK1 ubiquitin linkage composition. RIPK1 immunoprecipitates revealed that G1 and G15 markedly increased K48-linked ubiquitination while reducing basal K63-linked ubiquitination in PC-3 cells; BJ-2136 had little effect on either linkage (Fig. 5A, B). These changes coincided with increased RIPK1, RIPK3, and MLKL phosphorylation, without detectable FADD phosphorylation or caspase-8 activation (Fig. 5C).

G1- and G15-induced K48/K63 ubiquitination changes persisted after GPER depletion without significant differences from controls (Fig. 5D, E). RIPK1, RIPK3, and MLKL phosphorylation likewise remained detectable despite GPER depletion, whereas FADD phosphorylation and caspase-8 activation remained undetectable (Fig. 5F).

To determine whether RIPK1 ubiquitination could be modulated independently of GPER, we employed a cell-free system containing recombinant RIPK1, E1, E2, and the E3 ligase cIAP1 (Fig. 5G). G1 and G15 increased high-molecular-weight ubiquitin-positive species that were also recognized by an anti-RIPK1 antibody, consistent with enhanced RIPK1 ubiquitination. In contrast, BJ-2136 and CITFA reduced RIPK1 ubiquitination relative to the basal reaction. These findings demonstrate ligand-dependent modulation of RIPK1 ubiquitination in the absence of GPER, without establishing the linkage specificity of the ubiquitin chains formed.

To distinguish RIPK1 kinase-dependent necroptotic signaling from caspase-dependent signaling, we examined the effects of necrostatin-1 and z-VAD-fmk. Necrostatin-1 dose-dependently attenuated G1- and G15-induced RIPK1–RIPK3–MLKL phosphorylation, whereas z-VAD-fmk had no detectable effect (Fig. 5H). Necrostatin-1 also suppressed BiP and CHOP induction, and both necrostatin-1 and TUDCA reduced ligand-induced Annexin V^+/PI^+ populations, with greater protection afforded by necrostatin-1 (Fig. 5H, I). These findings implicate RIPK1 kinase activity in G1- and G15-induced cell death but do not establish that RIPK1 ubiquitin-chain remodeling causally drives this death. The GPER-independent component of ubiquitin remodeling is instead supported by the GPER-depletion and cell-free assays (Fig. 5D–G).

Functional characterization and predicted binding interactions of GPER ligands

We next distinguished receptor engagement from necroptotic signaling by assessing Ca^{2+} mobilization. G1 and BJ-2136 increased intracellular Ca^{2+} in PC-3 cells, with both responses markedly attenuated, but not abolished, by GPER knockdown (Fig. 6A). In COS-7-$GPER^{OV}$ cells, G1 and BJ-2136 elicited concentration-dependent Ca^{2+} mobilization with EC_{50} values of 1.11 ± 0.50 and 1.51 ± 0.50 μM, respectively (Fig. 6B). G15 (10 μM) shifted both concentration–response curves rightward, yielding apparent K_B estimates of 1.92 and 0.92 μM, respectively (Table 1). These single-concentration estimates do not establish equilibrium antagonist affinities or a specific antagonism mechanism.

To examine potential structural correlates of divergent G1 and BJ-2136 signaling, we docked both ligands into Lys05-bound GPER. Redocking of Lys05 partially reproduced its experimentally resolved binding pose, including interactions with Glu115 and Glu275, with a symmetry-corrected heavy-atom RMSD of 3.35 Å (Fig. 6C; Supplementary Table S1). GNINA docking predicted partially overlapping but distinct poses for BJ-2136, G1, and CITFA enantiomers within the Lys05-defined cavity (Fig. 6D–G; Supplementary Table S2). BJ-2136 and G1 occupied similar regions, although BJ-2136 exhibited a favorable predicted hydrogen-bond geometry with Glu115 that was absent in the selected G1 pose (Supplementary Figs. S1, S2). The CITFA enantiomers showed broadly similar orientations but differed in predicted polar interactions near Glu275 and Asn310 (Supplementary Fig. S3).

We also examined BJ-2136 analogues. Chlorine removal (BJ-2145) or replacement with bromine (BJ-21A05) reduced Ca^{2+} responses (Fig. 6H). Because both analogues also lack the fluorine substituent present in BJ-2136, these differences cannot be attributed solely to chlorine substitution.

Comparison with two apo-GPER water positions (PDB 8XOG) revealed distinct spatial relationships with predicted G1 and BJ-2136 poses (Supplementary Fig. S4A). G1 was positioned closer than BJ-2136 to the second mapped water site, suggesting different polar interaction environments. However, explicit water molecules were not included in docking, precluding conclusions about water occupancy or water-mediated hydrogen bonding. We also docked the antagonists G15 and G36 into the Lys05-defined cavity (Supplementary Fig. S4B). G15 exhibited a distinct predicted binding orientation (Supplementary Fig. S4C), whereas G36 largely overlapped with G1 (Supplementary Fig. S4D). Unlike G1, however, G36 lacks the acetyl oxygen positioned near the second mapped apo-water site, suggesting a potential difference in local polar interactions despite their similar predicted binding orientations (Supplementary Fig. S4E).

DISCUSSION

The present study identifies an unexpected functional interface between GPER pharmacology and RIPK1-dependent cell death. G1 and BJ-2136 exhibited agonist-like activity in GPER-mediated Ca^{2+} mobilization, whereas G15 displayed antagonist activity in this response, consistent with their established pharmacological classification. However, these ligands exhibited markedly divergent signaling outputs beyond Ca^{2+} mobilization. BJ-2136 robustly stimulated cAMP signaling without appreciable activation of necroptotic signaling, whereas G1 and G15 elicited little or no cAMP response but activated the RIPK1–RIPK3–MLKL axis and induced RIPK1-dependent cytotoxicity. Notably, G1 promoted the association of activated RIPK1, RIPK3, and MLKL with GPER, whereas G15 activated the same downstream pathway without detectable formation of a comparable GPER-associated complex. Together, these findings extend the conventional view of GPER pharmacology beyond rapid estrogen-responsive signaling [20] and

demonstrate that ligand classification based on conventional receptor responses does not necessarily predict downstream RIPK1 signaling or cell fate.

Our findings further suggest that GPER contributes to the basal regulation of RIPK1. RIPK1 protein stability is regulated, at least in part, by HSP90-dependent chaperone activity and proteasomal degradation [21]. Across the cellular models examined, higher GPER abundance was generally associated with increased RIPK1 protein and basal phosphorylation, whereas manipulation of GPER expression altered RIPK1 protein abundance without corresponding changes in RIPK1 mRNA. Matched-background cycloheximide experiments further showed modest but reproducible differences in relative RIPK1 persistence associated with GPER abundance. These observations support a post-transcriptional relationship between GPER and RIPK1, although they do not establish GPER as the sole determinant of RIPK1 stability. Moreover, basal RIPK1 phosphorylation was insufficient to elicit spontaneous necroptotic signaling, indicating that RIPK1 abundance and basal phosphorylation should be distinguished from the ligand-induced signaling events required to engage the RIPK3–MLKL pathway.

The dissociation between conventional GPER responses and RIPK1-dependent cell death raises an important distinction between ligand pharmacology and cell-death mechanisms. Although ligand-dependent differences in signaling are reminiscent of biased GPCR pharmacology [22], the persistence of RIPK1 responses following GPER depletion argues against interpreting these findings solely in terms of receptor-mediated signaling bias. Moreover, the transient RIPK1 phosphorylation induced by endogenous E2 without downstream RIPK3–MLKL activation indicates that RIPK1 phosphorylation alone is insufficient to define a necroptotic response.

Comparison with TNF-α further distinguished the G1-associated signaling architecture from canonical TNFR1-associated signaling complexes [23]. Although TNF-α activated RIPK1–RIPK3–MLKL signaling, its limited association with GPER contrasted with the prominent recovery of activated RIPK signaling components in GPER immunoprecipitates following G1 treatment. These

findings suggest that GPER-associated complex organization represents a ligand-selective feature rather than a general consequence of necroptotic pathway activation. Structure-guided docking provided a complementary framework for interpreting ligand recognition at GPER, while highlighting the distinction between predicted receptor interactions and experimentally observed cell-death responses. Using the experimentally resolved Lys05-bound GPER structure [16], we found that G1 and BJ-2136 occupied overlapping predicted binding regions but differed in their local polar interactions, whereas CITFA enantiomers exhibited distinct interaction geometries. Comparisons involving G15, G36, and apo-GPER water positions further suggested that local polar recognition, potentially involving water-mediated interactions, may contribute to ligand-dependent pharmacological activity. However, these interpretations remain hypothetical, particularly given the limitations of Lys05 redocking, the absence of explicit-water treatment, and the lack of experimental validation of the predicted ligand poses.

Importantly, the predicted ligand–receptor interactions should be distinguished from the mechanisms underlying RIPK1-dependent cell death. This distinction is particularly relevant because GPER depletion did not abolish G1- or G15-induced RIPK1 signaling, despite the GPER dependence of their conventional receptor-associated responses. Thus, the structural analyses provide testable hypotheses regarding ligand recognition, while leaving the proximal mechanisms of ligand-induced RIPK1 activation unresolved.

RIPK1 ubiquitination emerged as an additional layer of ligand-dependent regulation. Ubiquitin architecture is a major determinant of RIPK1 signaling, with K63- and M1-linked chains generally supporting signaling-complex organization and pro-survival responses, whereas disruption or remodeling of these scaffolds can facilitate RIPK1 kinase-dependent cell death [24–28]. G1 and G15 shifted RIPK1 ubiquitination toward increased K48- and reduced K63-linked species, whereas BJ-2136 largely preserved the basal pattern. Importantly, however, this remodeling cannot be attributed exclusively to GPER. GPER depletion did not significantly alter the G1- or

G15-induced changes in RIPK1 ubiquitination, and both ligands enhanced RIPK1 ubiquitination in a GPER-free system containing recombinant RIPK1, E1, E2, and cIAP1. These findings demonstrate that G1 and G15 can enhance RIPK1 ubiquitination in the absence of GPER, suggesting that GPER-independent mechanisms may also contribute to ligand-induced RIPK1 ubiquitin remodeling. The molecular target through which G1 and G15 influence the ubiquitination machinery remains unresolved, and the contribution of additional ubiquitin regulators, including A20 and CYLD [29, 30], warrants investigation. Furthermore, although RIPK1 ubiquitin remodeling closely accompanied necroptotic signaling, the present experiments do not establish that the K48/K63 shift itself is causally required for cell death.

The functional importance of RIPK1 kinase activity was nevertheless clear. Necrostatin-1 suppressed G1- and G15-induced RIPK1–RIPK3–MLKL activation, ER stress markers, and cell death, whereas pan-caspase inhibition had little effect. These observations, together with the absence of detectable caspase-8 activation and the increase in Annexin V^+/PI^+ cells, support a predominant contribution of RIPK1-dependent necroptotic signaling to G1- and G15-induced cell death. BiP and CHOP induction and the protective effect of the chemical chaperone TUDCA further indicate functional interaction between RIPK1-dependent death signaling and ER stress. Bidirectional crosstalk between necroptosis and ER stress has been described in other cellular contexts [31–33], although the sequence linking these pathways in GPER ligand-treated cells remains to be established.

Collectively, these findings distinguish three regulatory features of the GPER–RIPK1 relationship: basal regulation of RIPK1 abundance, ligand-selective organization of GPER-associated signaling complexes, and RIPK1 ubiquitin remodeling that can occur independently of GPER. This distinction challenges a simple receptor–effector interpretation of GPER ligand pharmacology and suggests that the mechanisms governing receptor activation and necroptotic cell fate are not necessarily shared.

MATERIALS AND METHODS

Cell culture

PC-3 and LNCaP were purchased from the Korean Cell Line Bank (Seoul, Korea). COS-7, HT-29, MCF-7, and U937 cell lines were obtained from the American Type Culture Collection (ATCC, Manassas, VA, USA). PC-3, HT-29, LNCaP, and U937 cells were cultured in RPMI-1640 medium, whereas COS-7 and MCF-7 cells were maintained in high-glucose Dulbecco's Modified Eagle Medium (DMEM). All culture media were supplemented with 10% fetal bovine serum (FBS). Cells were incubated in a humidified atmosphere at 37 °C with 5% CO_2.

GPER-expressing stable cell line generation

COS-7 cells stably overexpressing GPER were generated by transfecting cells with 5 μg of GPER (NM_001039966) Human Tagged ORF Clone plasmid (OriGene, Rockville, MD, USA) using Lipofectamine 3000 (Invitrogen, Carlsbad, CA, USA), according to the manufacturer's protocol provided in the OriGene transduction technical bulletin (RG203027). Following transfection, cells were cultured in DMEM supplemented with 10% fetal bovine serum (FBS) and 1 mg/mL neomycin for selection. Stable overexpression of GPER was confirmed by immunoblotting.

Reagents and antibodies

RPMI-1640, DMEM-HG media were purchased from Hyclone (Logan, UT, USA), and Opti-MEM, fetal bovine serum (FBS), penicillin/streptomycin were obtained from Gibco (Grand Island, NY, USA). GPER ligands G1 and G15 were sourced from R&D Systems (Minneapolis, MN, USA), while the compound BJ-2136 was synthesized in the laboratory of Professor Byeong-Seon Jeong

(College of Pharmacy, Yeungnam University, Republic of Korea). The chemical chaperone tauroursodeoxycholic acid (TUDCA) and the RIPK1 inhibitor Necrostatin-1 (Nec-1) were purchased from MedChemExpress (Princeton, NJ, USA). Antibodies against phospho-MLKL, BiP, CHOP, Ubiquitin, and K63-linked Ubiquitin were obtained from Cell Signaling Technology (Beverly, MA, USA). Antibodies against phospho-RIPK3 were obtained from Abcam (Cambridge, MA, USA), RIPK3 from Invitrogen (Carlsbad, CA, USA), and RIPK1, phospho-RIPK1, K48-linked ubiquitin and GPER from Abclonal (Woburn, MA, USA). Additional reagents used in this study included 3-(4,5-dimethylthiazol-2-yl)-2,5-diphenyltetrazolium bromide (MTT), Cycloheximide (CHX) from Sigma-Aldrich (St. Louis, MO, USA), the FITC Annexin V Apoptosis Detection Kit I from BD Biosciences (Bedford, MA, USA). Recombinant RIPK1 protein was purchased from ORIGENE (Rockville, MD, USA). Recombinant cIAP1 and Recombinant UBE2D2 were obtained from Abclonal (Woburn, MA, USA).

Cell viability and necroptosis assays

Cell viability was assessed using the 3-(4,5-dimethylthiazol-2-yl)-2,5-diphenyltetrazolium bromide (MTT) assay. Cells were seeded in 96-well plates and cultured in medium containing 1% FBS for 24 h. Cells were then treated with or without drugs in media containing 1% FBS. After 24 or 48 h, MTT solution (Merck, Burlington, MA, USA) was added to each well and incubated for 2 h. Following incubation, the MTT-containing medium was removed, and dimethyl sulfoxide (DMSO) was added to solubilize the formazan crystals. Absorbance was measured at 540 nm using a microplate reader (BMG LABTECH GmbH, Ortenberg, Germany).

Cell death was assessed using a FITC Annexin V apoptosis detection kit (BD Biosciences, San Jose, CA, USA) according to the manufacturer's instructions. Briefly, cells treated with the indicated compounds for 24 or 48 h were trypsinized and washed with ice-cold PBS. Cells (1×10^5) were

resuspended in 100 μL of 1× binding buffer and stained with 5 μL of Annexin V-FITC and 5 μL of propidium iodide (PI) for 15 min at 25 °C in the dark. Subsequently, 400 μL of 1× binding buffer was added, and the samples were analyzed by flow cytometry using a FACSVerse cytometer (BD Biosciences, San Jose, CA, USA). Annexin V^+/PI^+ and Annexin V^-/PI^+ cell populations were quantified, with the Annexin V^-/PI^+ population considered indicative of necrotic cell death.

Co-Immunoprecipitation (Co-IP) and Western blot analysis

For immunoprecipitation, 100 μg of total protein was incubated with an IP-grade antibody against GPER, RIPK1, or control IgG (1 mg/mL; Sigma-Aldrich) for 16 h at 4 °C. Subsequently, 50 μL of Protein G agarose beads (Thermo Scientific) were added to the mixture and incubated for an additional 4 h at 4 °C. Immune complexes were collected by centrifugation at 3,000 × g for 2 min at 4 °C, washed with PBS, and resuspended in 25 μL of 1× sample buffer (62.5 mM Tris-HCl pH 6.8, 2.5% SDS, 0.002% bromophenol blue, 5% β-mercaptoethanol, and 10% glycerol). Samples were heated at 95 °C for 5 min, followed by centrifugation at 12,000 × g for 30 s at 4 °C. The resulting supernatants were collected for SDS-PAGE and Western blot analysis.

For total protein extraction, cells were lysed using radioimmunoprecipitation assay (RIPA) buffer (Thermo Scientific, Waltham, MA, USA) supplemented with 1× protease and phosphatase inhibitor cocktail (Thermo Scientific). Proteins were separated by SDS-PAGE and transferred onto nitrocellulose membranes (Whatman GmbH, Dassel, Germany). Membranes were probed with specific primary and HRP-conjugated secondary antibodies, and immunoreactive bands were visualized using an enhanced chemiluminescence (ECL) detection kit (Thermo Scientific). Images were captured using the LAS-4000 mini imaging system (Fuji, Tokyo, Japan).

Denaturing immunoprecipitation for ubiquitination analysis

To detect ubiquitination of RIPK1 or GPER under conditions that disrupt non-covalent protein–protein interactions, immunoprecipitation was performed under denaturing conditions. Cells were lysed in buffer containing 1% SDS, and the lysates were heated at 95 °C for 5 min. The denatured lysates were then diluted with immunoprecipitation (IP) lysis buffer to reduce the final SDS concentration to approximately 0.1%. Equal amounts of protein were incubated with an antibody against RIPK1 or GPER for 16 h at 4 °C, followed by incubation with 50 μL of Protein G agarose beads for an additional 4 h at 4 °C. The immunoprecipitates were collected by centrifugation at 3,000 × g for 2 min at 4 °C and washed thoroughly with IP lysis buffer. The precipitated proteins were eluted in 1× sample buffer by heating at 95 °C for 5 min and analyzed by SDS-PAGE and Western blotting using antibodies against total ubiquitin, K48-linked ubiquitin, or K63-linked ubiquitin.

Quantitative Real-Time PCR (qPCR)

Total RNA was extracted from cells using TRIzol reagent (Ambion, Thermo Fisher Scientific, Waltham, MA, USA), following the manufacturer's protocol. Complementary DNA (cDNA) was synthesized from 1 μg of total RNA using the GoScript™ Reverse Transcriptase kit (Promega, Madison, WI, USA). Quantitative real-time PCR (qPCR) was performed using SYBR Green PCR Master Mix (QIAGEN, Valencia, CA, USA). The primers used for amplification were specific for the following genes: RIPK1 (forward: 5′-TATCCCAGTGCCTGAGACCAAC-3′, reverse: 5′-GTAGGCTCCAATCTGAATGCCAG-3′), GPER1 (forward: 5′-TTCCGCGAGAAGATGACCATCC-3′, reverse: 5′-TAGTACCGCTCGTGCAGGTTGA-3′), GAPDH (forward: 5′-ACCACAGTCCATGCCATCAC-3′, reverse: 5′-TCCACCACCCTGTTGCTGTA-3′). GAPDH was used as the housekeeping gene.

siRNA treatment

siRNA transfection followed the siRNA transfection application guide. Briefly, cells were seeded in antibiotic-free media and transfected with 100 nM siRNA targeting GPER or RIPK1 (ORIGENE, Rockville, MD, USA) for 72 h using Lipofectamine 3000 (Thermo Scientific, Waltham, MA, USA).

Cell-surface GPER antibody accessibility assay

PC-3 cells (1×10^4 cells/well) were seeded in 96-well plates in RPMI-1640 medium supplemented with 1% fetal bovine serum (FBS) and 1% penicillin/streptomycin (P/S) and incubated for 24 h at 37 °C. After incubation, cells were treated with a GPER primary antibody and incubated at 37 °C for 30 min. Following a PBS wash, cells were treated with drugs for various time points. Cells were then fixed with 4% paraformaldehyde for 10 min, washed, and incubated with an HRP-conjugated secondary antibody for 1 h at room temperature. After additional washes with PBS, HRP substrate was added and incubated for 20 min. The reaction was stopped with hydrochloric acid (HCl), and the absorbance was measured at 450 nm using a microplate reader (BMG LABTECH GmbH, Ortenberg, Germany). Changes in absorbance were interpreted as changes in the cell-surface accessibility of antibody-labeled GPER.

Protein Decay assay

Parental COS-7 cells, COS-7-GPER^{OV} cells, and PC-3 cells transfected with non-targeting control siRNA (siNT) or GPER-targeting siRNA (siGPER) were seeded in the corresponding culture media and allowed to adhere overnight. The medium was then replaced with the corresponding culture medium supplemented with 1% FBS and 1% P/S, and the cells were incubated overnight.

For the assessment of basal GPER and RIPK1 protein stability, COS-7, COS-7-GPER^{OV}, PC-3, and GPER-depleted PC-3 cells were treated with cycloheximide (CHX; 50 μg/mL) to inhibit de novo protein synthesis, without additional ligand treatment. Cell lysates were collected at the indicated

time points. To examine ligand-dependent regulation under translational blockade, PC-3 cells were pretreated with CHX (50 μg/mL) for 30 min, followed by treatment with G1, G15, or BJ-2136. Cell lysates were collected at the indicated time points after ligand treatment.

Protein extraction was performed using RIPA buffer supplemented with protease and phosphatase inhibitors. Western blot analysis was conducted using antibodies against GPER, RIPK1, and p-RIPK1, as appropriate. Changes in protein abundance were assessed by densitometric analysis of the immunoreactive bands.

Intracellular cAMP measurement

Intracellular cyclic AMP (cAMP) levels were quantified using a cAMP Direct Immunoassay Kit (Abcam, ab138880, Cambridge, UK) according to the manufacturer's instructions. Cells were seeded in culture plates and treated with the indicated compounds for 1 h, followed by lysis using the provided lysis buffer. Cell lysates and cAMP standards were added to anti-cAMP antibody-coated black 96-well plates. HRP-conjugated cAMP was then added to each well and incubated for 2 h at room temperature. After washing to remove unbound reagents, the fluorescent detection reagent (AbRed detector) was added and incubated according to the manufacturer's instructions. Fluorescence was measured at excitation/emission wavelengths of 540/590 nm using a FLUOstar Omega microplate reader (BMG LABTECH GmbH, Ortenberg, Germany). Forskolin-treated cells served as a positive control for cAMP induction.

***In vitro* ubiquitination assay**

The in vitro ubiquitination assay was performed using the Ubiquitylation Assay Kit (ab139467) according to the manufacturer’s instructions. Briefly, the ubiquitination reaction was assembled in a final volume of 50 μL containing E1 ubiquitin-activating enzyme (from assay kit), UBE2D2

(E2 ubiquitin-conjugating enzyme), recombinant cIAP1 (E3 ubiquitin ligase), ubiquitin, ATP/Mg^{2+} reaction buffer, and recombinant RIPK1 protein as the substrate. The reaction mixture was prepared on ice by sequentially adding ubiquitination buffer, ubiquitin, E1 enzyme, E2 enzyme, and cIAP1, followed by recombinant RIPK1 protein.

To examine the effects of GPER-related ligands on RIPK1 ubiquitination, the small-molecule compounds G1, G15, BJ-2136, and CITFA were added to the reaction mixture at the indicated concentrations prior to incubation. Control reactions without compounds were included in parallel.

The reaction was initiated by the addition of ATP and incubated at 37 °C for 3 h to allow ubiquitin conjugation. Control reactions lacking E1, E2, E3, or ATP were included to confirm the specificity of the ubiquitination reaction. Following incubation, the reactions were terminated by adding SDS loading buffer and heating at 95 °C for 5 min. The reaction products were resolved by SDS–PAGE and analyzed by immunoblotting using anti-ubiquitin and anti-RIPK1 antibodies.

Measurement of Intracellular Ca^{2+} Levels

Cells were seeded in black 96-well plates at a density of 1×10^4 cells per well and incubated for 24 h to allow attachment. Cells were labeled with 1 μM Indo-1 AM (Invitrogen, Carlsbad, CA, USA) for 30 min and subsequently treated with the indicated drugs for 3 h. Indo-1 fluorescence was measured using a FLUOstar Omega plate reader at an excitation wavelength of 355 nm and an emission wavelength of 460 nm. Fluorescence responses were normalized to vehicle-treated controls.

Protein preparation

The cryo-EM structure of human GPER–Gq bound to Lys05 (PDB 8XOF) was used as the receptor template. GPER chain R was extracted and prepared using DeepZema® (Innovo Therapeutics, Republic of Korea). Missing heavy atoms in experimentally observed residues were reconstructed using PDBFixer [34] and subjected to local geometry optimization with the AMBER14 force field in OpenMM [35]. Hydrogens were added at pH 7.4, with automatic histidine protonation-state assignment and restrained energy minimization while preserving the experimentally determined heavy-atom coordinates. The resolved Lys05 ligand (CCD A1LVW) defined the docking site and was subsequently removed. Pocket water molecules were not retained.

Ligand preparation

BJ-2136, G1, CITFA, G15, and G36 were prepared from SMILES using Schrödinger LigPrep with EpikX [36] and the OPLS4 force field. Protonation and tautomeric states were evaluated at pH 7.4 ± 1.0, and stereochemical configurations were retained. A single neutral species was obtained for BJ-2136 and G1. Because CITFA was used as a C-2 racemate, both enantiomers were generated and independently docked. Lys05 was separately prepared for redocking, yielding six protonation states.

Molecular docking

Molecular docking was performed using GNINA (v1.3.2-2-gd33747d6) [37] through the DeepZema platform with an NVIDIA RTX PRO 6000 GPU. The Lys05-defined search box was centered on the midpoint of the resolved ligand coordinate ranges, with 5 Å padding and a minimum dimension of 20 Å (final dimensions, 20 × 20 × 25.3 Å). Settings were identical across ligands: exhaustiveness 256, random seed 42, and up to 10 output poses. CNN rescoring was used to rank empirically generated poses. For redocking validation, the Lys05 state most closely

reproducing the experimental pose was compared by symmetry-corrected heavy-atom RMSD without further ligand alignment.

Docking result analysis

Predicted ligand–GPER complexes were visualized using PyMOL. Hydrogen bonds were evaluated by hydrogen-to-acceptor distances and donor–hydrogen–acceptor angles; aromatic and nonpolar contacts were assessed geometrically, with residues within 5.5 Å considered for binding-site vicinity. The highest CNN-scoring pose of each ligand species was selected. Two water positions in apo-GPER (PDB 8XOG) were transferred to the 8XOF coordinate frame after protein alignment using US-align (Cα RMSD, 0.76 Å over 265 residues), and interatomic distances were measured. These positions were used only as structural references; explicit-water docking was not performed.

Water analysis

The apo structure 8XOG was superposed onto the Lys05-bound structure 8XOF using US-align (version 20261019) [38]. The two structures aligned with a Cα RMSD of 0.76 Å over 265 residues and a TM-score of 0.96, indicating essentially identical backbone conformations. The two ordered water molecules present in 8XOG (occupancy 1.0, B-factor 30) were transferred into the 8XOF frame, and distances from these positions to Lys05 and to the docked poses of BJ-2136 and G1 were measured in that frame.

Statistical analysis

All experiments were independently performed three times (n = 3). Data are presented as mean

± SEM. Statistical significance was assessed by one-way analysis of variance (ANOVA) followed by Tukey's multiple comparison, using GraphPad Prism 8.0 (San Diego, CA, USA). A P value < 0.05 was considered statistically significant.

Acknowledgements

This work was supported by grants from the National Research Foundation of Korea (NRF), funded by the Korean government (MSIT), Republic of Korea (Grant No.: NRF-2023R1A2C1006689, RS-2026-25588840).

Author contributions

Kiran Yadav: Methodology, Investigation, Visualization, Formal analysis, Data curation. **Kalpana Ghimire:** Investigation, Visualization, Formal analysis, Data curation. **Hee Dong Park**: Methodology, Investigation. **Dongchul Lim**: Writing – review & editing, Writing – original draft. Methodology, Visualization, Formal analysis, **Byeong-Seon Jeong:** Writing – review & editing, Writing – original draft, Resources, Funding acquisition, Formal analysis, Data curation, Conceptualization. **Jung-Ae Kim:** Writing – review & editing, Writing – original draft, Visualization, Supervision, Methodology, Funding acquisition, Formal analysis, Data curation, Conceptualization.

Competing interests

The authors declare no competing interests.

References

1. Galluzzi L, Vitale I, Aaronson SA, Abrams JM, Adam D, Agostinis P, et al. Molecular mechanisms of cell death: recommendations of the Nomenclature Committee on Cell Death 2018. *Cell Death*

598 *Differ* **25**(3), 486-541 (2018).

599 2. Gong Y, Fan Z, Luo G, Yang C, Huang Q, Fan K, et al. The role of necroptosis in cancer biology and
600 therapy. *Mol Cancer* **18**(1),100 (2019).

601 3. Strilic B, Yang L, Albarrán-Juárez J, Wachsmuth L, Han K, Müller UC, et al. Tumour-cell-induced
602 endothelial cell necroptosis via death receptor 6 promotes metastasis. *Nature* **536**(7615), 215-
603 8 (2016).

604 4. Dhillon AS, Hagan S, Rath O, Kolch W. MAP kinase signalling pathways in cancer. *Oncogene*
605 **26**(22), 3279-90 (2007).

606 5. Porta C, Paglino C, Mosca A. Targeting PI3K/Akt/mTOR Signaling in Cancer. *Front Oncol* **4**, 64
607 (2014).

608 6. Ofengeim D, Yuan J. Regulation of RIP1 kinase signalling at the crossroads of inflammation and
609 cell death. *Nat Rev Mol Cell Biol* **14**(11), 727-36 (2013).

610 7. Xu D, Zou C, Yuan J. Genetic Regulation of RIPK1 and Necroptosis. *Annu Rev Genet* **55**, 235-63
611 (2021).

612 8. Najafov A, Mookhtiar AK, Luu HS, Ordureau A, Pan H, Amin PP, et al. TAM Kinases Promote
613 Necroptosis by Regulating Oligomerization of MLKL. *Molecular Cell* **75**(3), 457-68.e4 (2019).

614 9. Prossnitz ER, Barton M. The G-protein-coupled estrogen receptor GPER in health and disease.
615 *Nat Rev Endocrinol* **7**(12), 715-26 (2011).

616 10. Yan Y, Jiang X, Zhao Y, Wen H, Liu G. Role of GPER on proliferation, migration and invasion
617 in ligand-independent manner in human ovarian cancer cell line SKOV3. *Cell Biochem Funct*
618 **33**(8), 552-9 (2015).

619 11. Cirillo F, Talia M, Santolla MF, Pellegrino M, Scordamaglia D, Spinelli A, et al. GPER deletion
620 triggers inhibitory effects in triple negative breast cancer (TNBC) cells through the JNK/c-

Jun/p53/Noxa transduction pathway. *Cell Death Discov* **9**(1), 353 (2023).

12. Bologa CG, Revankar CM, Young SM, Edwards BS, Arterburn JB, Kiselyov AS, et al. Virtual and biomolecular screening converge on a selective agonist for GPR30. *Nat Chem Biol* **2**(4), 207-12 (2006).

13. Dennis MK, Burai R, Ramesh C, Petrie WK, Alcon SN, Nayak TK, et al. In vivo effects of a GPR30 antagonist. *Nat Chem Biol* **5**(6), 421-7 (2009).

14. Luo H, Yang G, Yu T, Luo S, Wu C, Sun Y, et al. GPER-mediated proliferation and estradiol production in breast cancer-associated fibroblasts. *Endocr Relat Cancer* **21**(2), 355-69 (2014).

15. Vo DH, Hartig R, Weinert S, Haybaeck J, Nass N. G-Protein-Coupled Estrogen Receptor (GPER)-Specific Agonist G1 Induces ER Stress Leading to Cell Death in MCF-7 Cells. *Biomolecules* **9**(9), 503 (2019).

16. Liu H, Guo S, Dai A, Xu P, Li X, Huang S, et al. Structural and functional evidence that GPR30 is not a direct estrogen receptor. *Cell Res* **34**(7), 530-3 (2024).

17. Kaneda S, Jo-Watanabe A, Akasaka H, Oshima HS, Yokomizo T, Shihoya W, Nureki O. Cryo-EM structure of the bicarbonate receptor GPR30. *eLife* **13**, RP99874 (2026).

18. Awasthi BP, Chaudhary P, Lim D, Yadav K, Lee IH, Banskota S, et al. G Protein-Coupled Estrogen Receptor-Mediated Anti-Inflammatory and Mucosal Healing Activity of a Trimethylpyridinol Analogue in Inflammatory Bowel Disease. *J Med Chem* **67**(13), 10601-21 (2024).

19. Gaddum JH. The quantitative effects of antagonistic drugs. *J Physiol* **89**(1), 7-9 (1937).

20. Filardo E, Quinn J, Pang Y, Graeber C, Shaw S, Dong J, et al. Activation of the novel estrogen receptor G protein-coupled receptor 30 (GPR30) at the plasma membrane. *Endocrinology* **148**(7), 3236-45 (2007).

21. Vanden Berghe T, Kalai M, van Loo G, Declercq W, Vandenabeele P. Disruption of HSP90 function reverts tumor necrosis factor-induced necrosis to apoptosis. J Biol Chem **278**(8), 5622–5629 (2003).

22. Kenakin T, Christopoulos A. Signalling bias in new drug discovery: detection, quantification and therapeutic impact. *Nat Rev Drug Discov* **12**(3), 205-16 (2013).

23. Micheau O, Tschopp J. Induction of TNF receptor I-mediated apoptosis via two sequential signaling complexes. *Cell* **114**(2), 181-90 (2003).

24. Newton K. RIPK1 and RIPK3: critical regulators of inflammation and cell death. *Trends Cell Biol* **25**(6), 347-53 (2015).

25. Peltzer N, Darding M, Walczak H. Holding RIPK1 on the Ubiquitin Leash in TNFR1 Signaling. *Trends Cell Biol* **26**(6), 445-61 (2016).

26. Walczak H, Iwai K, Dikic I. Generation and physiological roles of linear ubiquitin chains. *BMC Biol* **10**, 23 (2012).

27. Ikeda F, Deribe YL, Skånland SS, Stieglitz B, Grabbe C, Franz-Wachtel M, et al. SHARPIN forms a linear ubiquitin ligase complex regulating NF-κB activity and apoptosis. *Nature* **471**(7340), 637-41 (2011).

28. Tang Y, Tu H, Zhang J, Zhao X, Wang Y, Qin J, Lin X. K63-linked ubiquitination regulates RIPK1 kinase activity to prevent cell death during embryogenesis and inflammation. *Nat Commun* **10**, 4157 (2019).

29. Wertz IE, O'Rourke KM, Zhou H, Eby M, Aravind L, Seshagiri S, et al. De-ubiquitination and ubiquitin ligase domains of A20 downregulate NF-κB signalling. *Nature* **430**(7000), 694-9 (2004).

30. Moquin DM, McQuade T, Chan FK. CYLD deubiquitinates RIP1 in the TNFα-induced

667 necrosome to facilitate kinase activation and programmed necrosis. *PLoS One* **8**(10), e76841
668 (2013).

669 31. Zhu P, Hu S, Jin Q, Li D, Tian F, Toan S, et al. Ripk3 promotes ER stress-induced necroptosis
670 in cardiac IR injury: A mechanism involving calcium overload/XO/ROS/mPTP pathway. *Redox*
671 *Biol* **16**, 157-68 (2018).

672 32. Saveljeva S, Mc Laughlin SL, Vandenabeele P, Samali A, Bertrand MJ. Endoplasmic
673 reticulum stress induces ligand-independent TNFR1-mediated necroptosis in L929 cells. *Cell*
674 *Death Dis* **6**(1), e1587 (2015).

675 33. Grootjans J, Kaser A, Kaufman RJ, Blumberg RS. The unfolded protein response in
676 immunity and inflammation. *Nat Rev Immunol* **16**(8), 469-84 (2016).

677 34. Eastman P, and Pande V. PDBFixer: An open-source package for the preparation of
678 biomolecular structures for molecular simulations. Version 1.4. (2017)
679 https://github.com/openmm/pdbfixer.

680 35. Eastman P, Swails J, Chodera JD, McGibbon RT, Zhao Y, Beauchamp KA, Wang LP,
681 Simmonett AC, Harrigan MP, Stern CD, Wiewiora RP, Brooks BR, Pande VS. OpenMM 7: Rapid
682 development of high-performance algorithms for molecular dynamics. *PLoS Comput Biol* **13**(7),
683 e1005659 (2017).

684 36. Johnston RC, Yao K, Kaplan Z, Chelliah M, Leswing K, Seekins S, Watts S, Calkins D, Chief
685 Elk J, Jerome SV, Repasky MP, Shelley JC. Epik: pKa and protonation state prediction through
686 machine learning. *J Chem Theory Comput* **19**(8), 2380–2388 (2023).

687 37. McNutt AM, Li Y, Meli R, Aggarwal R, Koes DR. GNINA 1.3: the next increment in molecular
688 docking with deep learning. *J Cheminform* **17**, 28 (2025).

689 38. Zhang C, Shine M, Pyle AM, Zhang Y. US-align: universal structure alignments of proteins,

690 nucleic acids, and macromolecular complexes. *Nat Methods* **19**(9), 1109–1115 (2022).

691

Figure Legends

Fig. 1. Relationship between GPER expression and basal RIPK1 abundance and phosphorylation. A Basal expression of GPER, RIPK1, and phosphorylated RIPK1 (p-RIPK1) across cancer and non-cancer cell lines, including GPER-overexpressing COS-7 cells (COS-7-GPER^{OV}). PC-3 and LNCaP, human prostate cancer cell lines; HT-29, human colon cancer cell line; MCF-7, human breast cancer cell line; U937, human pro-monocytic leukemia cell line; COS-7, African green monkey kidney-derived fibroblast-like cell line. $^{*}P < 0.05$ versus COS-7 cells. **B-C** Quantification of basal GPER and RIPK1 protein (B) and mRNA (C) levels in COS-7, COS-7-GPER^{OV}, and GPER-depleted COS-7-GPER^{OV} cells. $^{*}P < 0.05$ versus vehicle-treated control group. $^{\#}P < 0.05$ versus COS-7-GPER^{OV} cells. **D** CHX chase analysis of GPER and RIPK1 protein stability in COS-7, COS-7-GPER^{OV}, PC-3, and GPER-depleted PC-3 cells (PC-3^{siGPER}). $^{*}P < 0.05$ versus the corresponding GPER at 24 h. **E** Effects of RIPK1 knockdown on G1-, G15-, and BJ-2136–induced cytotoxicity in COS-7, COS-7-GPER^{OV}, PC-3, and PC-3^{siGPER} cells. $^{*}P < 0.05$ versus BJ-2136-treated si*NT*-transfected group. $^{\#}P < 0.05$ versus the corresponding G1- or G15-treated si*NT*-transfected group. **F** Representative merged phase-contrast (P/C) and PI fluorescence images and quantification of PI-positive cells in PC-3 cells treated with G1, G15, or BJ-2136. PI, propidium iodide. Data represent mean ± SEM from three independent experiments. PI-positive cells were quantified from five randomly selected fields per experiment. $^{*}P < 0.05$ versus vehicle-treated control group.

Fig. 2. Differential effects of GPER ligands on RIPK1 regulation and cytotoxicity. A Chemical structures of the compounds shown in this figure. **B** Cytotoxic effects in PC-3 cells treated with G1, G15, BJ-2136, CITFA, or CIMBA. $^{*}P < 0.05$ versus BJ-2136-treated group. **C** Immunoblot analysis of GPER, RIPK1, and p-RIPK1 in PC-3 cells following treatment with G1, G15, BJ-2136, CITFA, or

CIMBA. $^{*}P < 0.05$ versus vehicle-treated control group. **D–E** Relative mRNA levels of GPER (D) and RIPK1 (E) in PC-3 cells treated with G1, G15, or BJ-2136 in the presence or absence of actinomycin D (ActD). $^{*}P < 0.05$ versus untreated control at 0 h. $^{\#}P < 0.05$ versus the corresponding ActD-untreated group. **F** Time-course immunoblot analysis of GPER, RIPK1, and p-RIPK1 in vehicle-treated PC-3 cells over 24 h. $^{*}P < 0.05$ versus 0 h control group. **G** Immunoblot analysis of GPER and RIPK1 in PC-3 cells treated with G1, G15, or BJ-2136 in the presence or absence of cycloheximide (CHX). $^{*}P < 0.05$ versus untreated control at 0 h. $^{\#}P < 0.05$ versus the corresponding CHX-untreated group. Data are presented as mean ± SEM from three independent experiments (n = 3).

Fig. 3. Ligand-dependent differences in GPER-associated complex formation and RIPK1 signaling. A Immunoblot analysis of GPER, RIPK1, and p-RIPK1 in PC-3 cells treated with G1, G15, or BJ-2136 in the presence or absence of MG-132. $^{*}P < 0.05$ versus vehicle-treated control group. $^{\#}P < 0.05$ versus BJ-2136-treated group. **B-C** Co-immunoprecipitation analysis of GPER and phosphorylated RIPK3 associated with RIPK1 in PC-3 (B) and COS-7-GPER^{OV} (C) cells following treatment with G1, G15, or BJ-2136. **D** Intracellular cAMP levels in PC-3 cells following treatment with G1, G15, BJ-2136, CITFA, or CIMBA, with forskolin included as a positive control. $^{*}P < 0.05$ versus vehicle-treated control group. $^{\#}P < 0.05$ versus forskolin-treated group. $^{\&}P < 0.05$, versus BJ-2136-treated group. **E** Immunoblot analysis of p-RIPK3 and p-MLKL in PC-3 cells treated with G1 or G15 following GPER knockdown. **F** Flow cytometric analysis and quantification of Annexin V^{+}/PI^{+} cells and Annexin V^{-}/PI^{+} cells in PC-3 cells treated with G1, G15, or BJ-2136 for 24 or 48 h. $^{*}P < 0.05$ versus vehicle-treated control group. $^{\#}P < 0.05$ versus G1-treated group. **G** Immunoblot analysis of the ER stress markers BiP and CHOP in PC-3 cells treated with increasing concentrations of G1 or G15. $^{*}P < 0.05$ versus the vehicle-treated control group. **H** Immunoblot analysis of whole-cell lysates (input) and GPER immunoprecipitates for RIPK1, RIPK3, MLKL,

FADD, and caspase-8 and their corresponding phosphorylated forms in PC-3 cells treated with G1, G15, or BJ-2136 in the presence or absence of TNF-α. $^{*}P < 0.05$ versus vehicle-treated control group (without TNF-α). $^{\#}P < 0.05$ versus the corresponding TNF-α-untreated group. **I** Time-course immunoblot analysis of GPER and RIPK1–RIPK3–MLKL signaling in PC-3 cells following stimulation with 17β-estradiol (E2), an endogenous estrogen. $^{*}P < 0.05$ versus vehicle-treated control group. Data are presented as mean ± SEM from three independent experiments (n = 3).

Fig. 4. Ligand-specific remodeling of GPER- and RIPK1-associated ubiquitination. A–C Immunoblot analysis of total ubiquitination in GPER and RIPK1 immunoprecipitates from PC-3 cells following treatment with G1 (A), BJ-2136 (B), or G15 (C). **D** Analysis of cell-surface GPER antibody accessibility in PC-3 cells following treatment with G1, BJ-2136, or G15. $^{*}P < 0.05$ versus untreated control or G15-treated group at the corresponding time point. **E–F** Immunoblot analysis of K48-linked (E) and K63-linked (F) ubiquitination in GPER immunoprecipitates from PC-3 cells treated with G1, G15, or BJ-2136. $^{*}P < 0.05$ versus untreated control at 0 h. $^{\#}P < 0.05$ versus the corresponding G1- or BJ-2136-treated group at 0.25 h. Data are presented as mean ± SEM from three independent experiments (n = 3).

Fig. 5. Ligand-specific RIPK1 ubiquitin remodeling and RIPK1-dependent necroptotic signaling. A–B Immunoblot analysis of K48-linked (A) and K63-linked (B) ubiquitin in RIPK1 immunoprecipitates from si*NT*-transfected PC-3 cells treated with G1, G15, or BJ-2136. **C** Immunoblot analysis of p-RIPK1, p-RIPK3, p-MLKL, caspase-8, and p-FADD in the corresponding whole-cell lysates from si*NT*-transfected PC-3 cells. **D–E** Immunoblot analysis of K48-linked (D) and K63-linked (E) ubiquitin in RIPK1 immunoprecipitates from si*GPER*-transfected PC-3 cells treated with G1, G15, or BJ-2136. K48- and K63-linked ubiquitination was quantified by densitometry and normalized to the corresponding immunoprecipitated RIPK1 signal. $^{*}P < 0.05$

versus 0 h within the corresponding treatment group. **F** Immunoblot analysis of p-RIPK1, p-RIPK3, p-MLKL, caspase-8, and p-FADD in the corresponding whole-cell lysates from si*GPER*-transfected PC-3 cells. **G** In vitro ubiquitination assay assessing the effects of G1, G15, BJ-2136, and CITFA on RIPK1 ubiquitination. Following immunoblotting with an anti-ubiquitin antibody, the same membrane was stripped and reprobed with an anti-RIPK1 antibody. An additional p-RIPK1 immunoblot is shown. High-molecular-weight RIPK1 species corresponding to the ubiquitin-positive smear are indicated. **H** Immunoblot analysis of p-RIPK1, p-RIPK3, and p-MLKL, together with the ER stress markers BiP and CHOP, in PC-3 cells treated with G1 or G15 (10 μM) in the presence of Nec-1 (3, 10, or 30 μM) or z-VAD (30 μM), with corresponding quantification of p-RIPK1, p-RIPK3, and p-MLKL levels. $^{*}P < 0.05$ versus vehicle-treated control group. $^{\#}P < 0.05$ versus the corresponding G1- or G15-treated group. **I** Flow cytometric analysis of Annexin V^{+}/PI^{+} cells and Annexin V^{-}/PI^{+} necrotic cells in PC-3 cells treated with G1 or G15 in the presence or absence of TUDCA or Nec-1, with corresponding quantification. $^{*}P < 0.05$ versus the untreated control group. $^{\#}P < 0.05$ versus the corresponding G1- or G15-treated group. Data are presented as mean ± SEM from three independent experiments (n = 3).

Fig. 6. GPER-dependent calcium mobilization and predicted binding interactions of GPER ligands. A Intracellular Ca^{2+} responses to G1 and BJ-2136 in PC-3 cells transfected with control siRNA (siNT) or GPER-targeting siRNA (siGPER). $^{*}P < 0.05$ versus drug-untreated control group. $^{\#}P < 0.05$ versus siNT-treated group. **B** Concentration–response curves for G1 and BJ-2136 in GPER-overexpressing COS-7 cells in the absence or presence of G15 (10 μM). $^{*}P < 0.05$ versus vehicle-treated control group. $^{\#}P < 0.05$ versus the corresponding G15-untreated group at the same agonist concentration. **C** Redocking of Lys05 into the experimentally defined GPER binding cavity. The symmetry-corrected heavy-atom RMSD between the experimentally resolved Lys05 pose (gray) and the redocked pose of Lys05 species 2 (magenta) was 3.35 Å, calculated without

additional ligand alignment. The predicted N–H···O(Glu115) interaction has an H···O distance of 2.08 Å and an N–H···O angle of 139.1°. The corresponding values for the predicted N–H···O(Glu275) interaction are 1.83 Å and 167.4°, respectively. **D** The chemical structures of BJ-2136, G1, and CITFA. **E–G** Spatial overlap of selected predicted poses for Lys05, BJ-2136 (E), G1 (F), and (S)-CITFA (G) within the experimentally defined binding cavity. **H** Intracellular Ca^{2+} responses to the structurally related compounds BJ-21A05 and BJ-2145 at 10 μM. $^{*}P < 0.05$ versus vehicle-treated control group.

Fig. 1

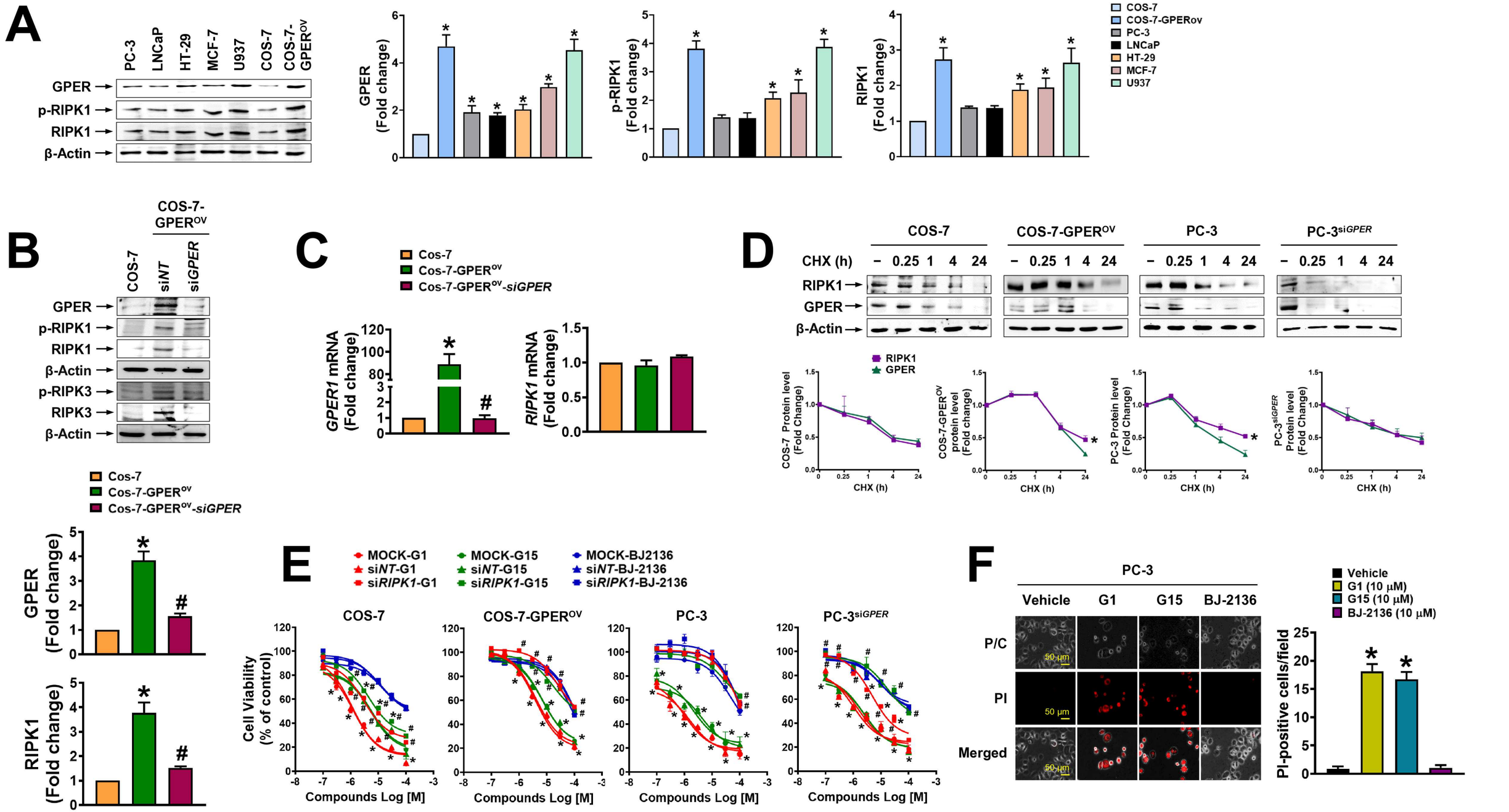
A
PC-3
LNCaP
HT-29
MCF-7
U937
COS-7
COS-7-GPER^OV
GPER
p-RIPK1
RIPK1
β-Actin
GPER (Fold change)
p-RIPK1 (Fold change)
RIPK1 (Fold change)
COS-7
COS-7-GPERov
PC-3
LNCaP
HT-29
MCF-7
U937
B
COS-7-GPER^OV
COS-7
siNT
siGPER
GPER
p-RIPK1
RIPK1
β-Actin
p-RIPK3
RIPK3
β-Actin
Cos-7
Cos-7-GPER^OV
Cos-7-GPER^OV-siGPER
GPER (Fold change)
RIPK1 (Fold change)
C
Cos-7
Cos-7-GPER^OV
Cos-7-GPER^OV-siGPER
GPER1 mRNA (Fold change)
RIPK1 mRNA (Fold change)
D
COS-7
COS-7-GPER^OV
PC-3
PC-3^siGPER
CHX (h)
– 0.25 1 4 24
RIPK1
GPER
β-Actin
RIPK1
GPER
COS-7 Protein level (Fold Change)
COS-7-GPER^OV protein level (Fold change)
PC-3 Protein level (Fold Change)
PC-3^siGPER Protein level (Fold Change)
CHX (h)
E
MOCK-G1
siNT-G1
siRIPK1-G1
MOCK-G15
siNT-G15
siRIPK1-G15
MOCK-BJ2136
siNT-BJ-2136
siRIPK1-BJ-2136
COS-7
COS-7-GPER^OV
PC-3
PC-3^siGPER
Cell Viability (% of control)
Compounds Log [M]
F
PC-3
Vehicle
G1
G15
BJ-2136
P/C
PI
Merged
50 μm
Vehicle
G1 (10 μM)
G15 (10 μM)
BJ-2136 (10 μM)
PI-positive cells/field

Fig. 2

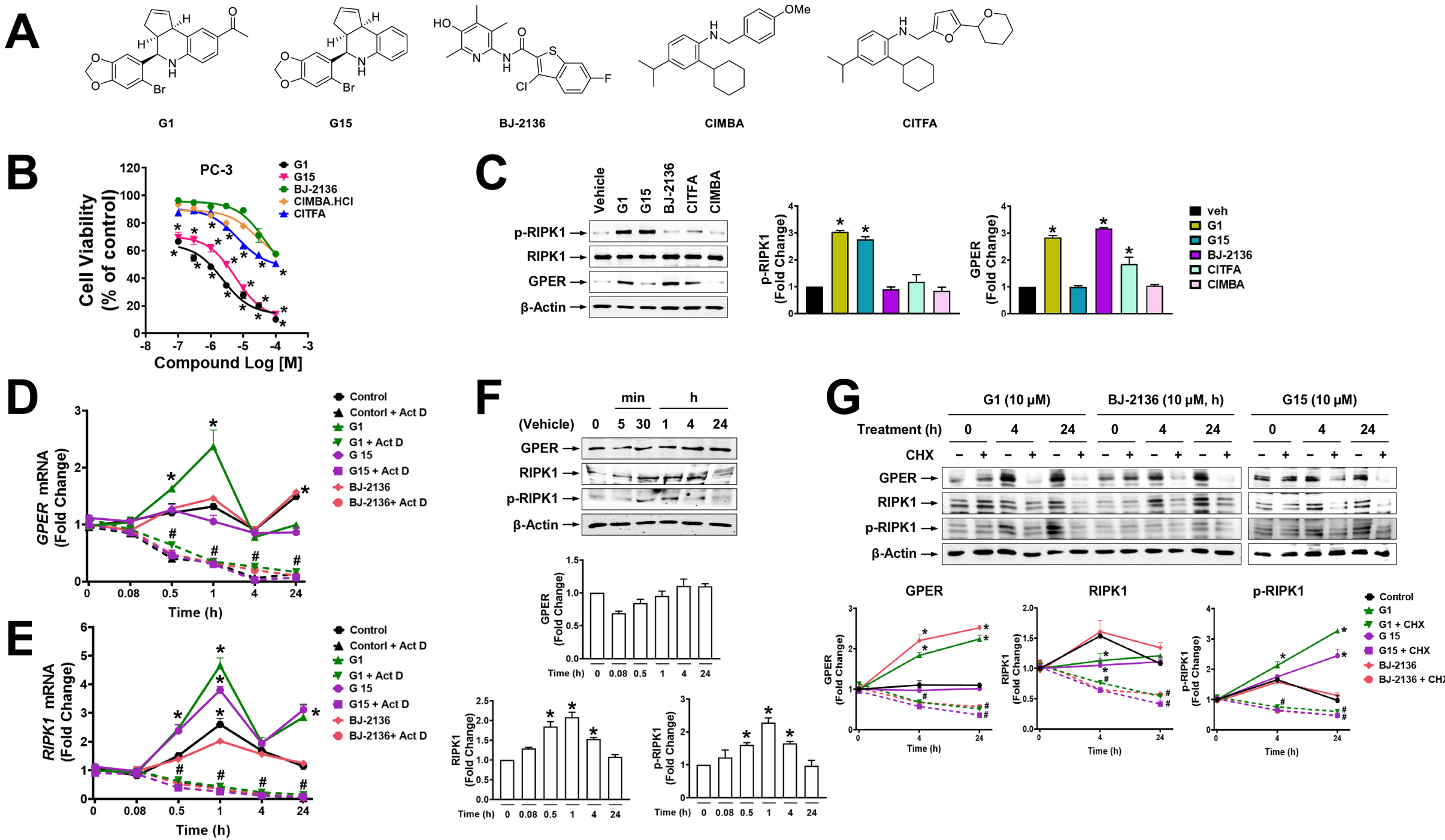
A
G1
G15
BJ-2136
CIMBA
CITFA
B
PC-3
G1
G15
BJ-2136
CIMBA.HCl
CITFA
Cell Viability (% of control)
Compound Log [M]
C
Vehicle
G1
G15
BJ-2136
CITFA
CIMBA
p-RIPK1 →
RIPK1 →
GPER →
β-Actin →
p-RIPK1 (Fold Change)
GPER (Fold Change)
veh
G1
G15
BJ-2136
CITFA
CIMBA
D
GPER mRNA (Fold Change)
Time (h)
Control
Contorl + Act D
G1
G1 + Act D
G 15
G15 + Act D
BJ-2136
BJ-2136+ Act D
E
RIPK1 mRNA (Fold Change)
Time (h)
Control
Contorl + Act D
G1
G1 + Act D
G 15
G15 + Act D
BJ-2136
BJ-2136+ Act D
F
min
h
(Vehicle) 0 5 30 1 4 24
GPER →
RIPK1 →
p-RIPK1 →
β-Actin →
GPER (Fold Change)
RIPK1 (Fold Change)
p-RIPK1 (Fold Change)
Time (h) 0 0.08 0.5 1 4 24
G
G1 (10 μM)
BJ-2136 (10 μM, h)
G15 (10 μM)
Treatment (h) 0 4 24 0 4 24 0 4 24
CHX – + – + – + – + – + – + – + – + – +
GPER →
RIPK1 →
p-RIPK1 →
β-Actin →
GPER
RIPK1
p-RIPK1
Time (h)
Control
G1
G1 + CHX
G 15
G15 + CHX
BJ-2136
BJ-2136 + CHX

Fig. 3

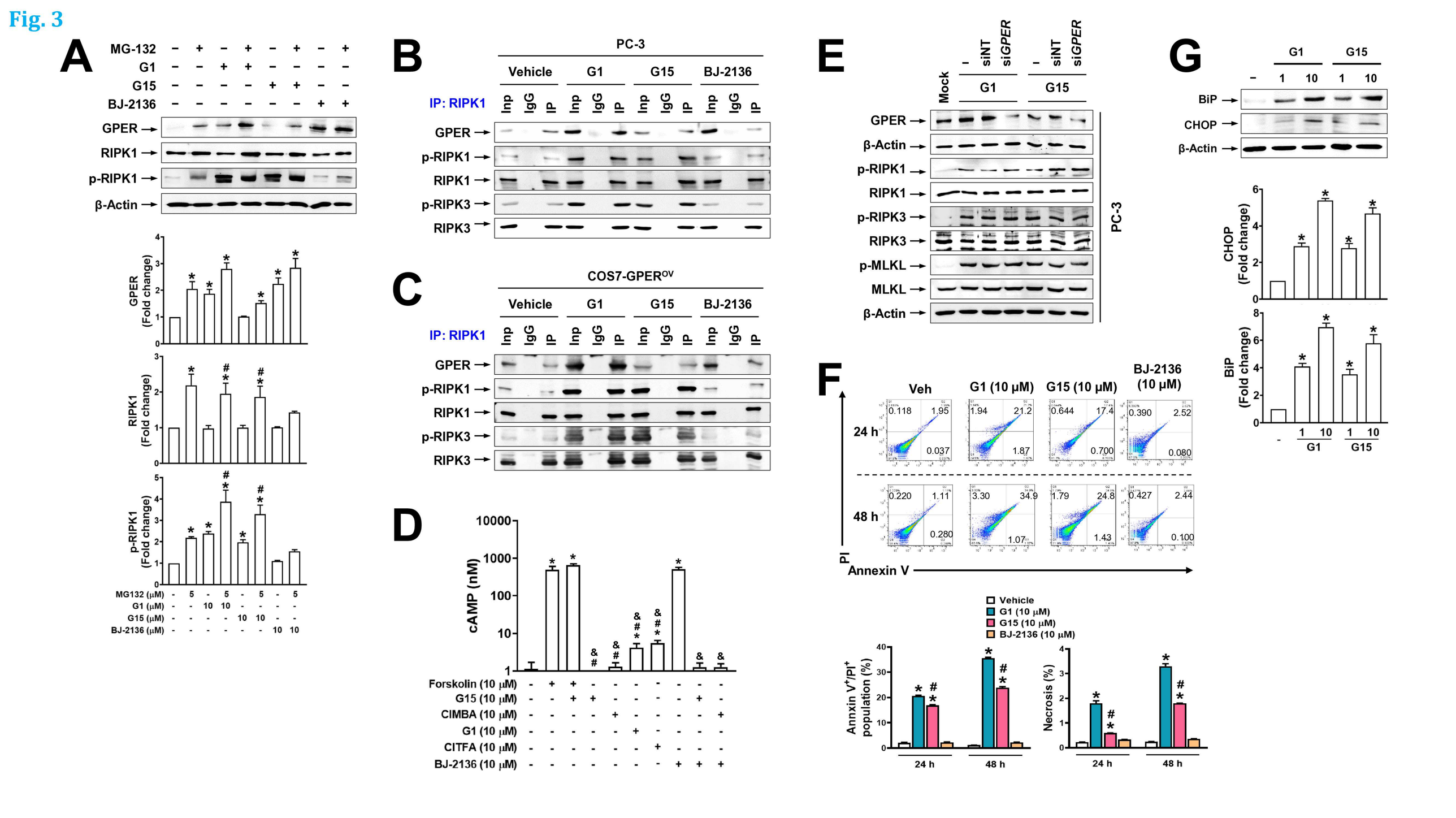
A
MG-132
G1
G15
BJ-2136
GPER
RIPK1
p-RIPK1
β-Actin
GPER (Fold change)
RIPK1 (Fold change)
p-RIPK1 (Fold change)
MG132 (μM)
G1 (μM)
G15 (μM)
BJ-2136 (μM)
B
PC-3
Vehicle
G1
G15
BJ-2136
IP: RIPK1
Inp
IgG
IP
GPER
p-RIPK1
RIPK1
p-RIPK3
RIPK3
C
COS7-GPER^OV
D
cAMP (nM)
Forskolin (10 μM)
G15 (10 μM)
CIMBA (10 μM)
G1 (10 μM)
CITFA (10 μM)
BJ-2136 (10 μM)
E
Mock
siNT
siGPER
PC-3
p-MLKL
MLKL
F
Veh
G1 (10 μM)
G15 (10 μM)
BJ-2136 (10 μM)
24 h
48 h
PI
Annexin V
Vehicle
G1 (10 μM)
G15 (10 μM)
BJ-2136 (10 μM)
Annxin V+/PI+ population (%)
Necrosis (%)
G
BiP
CHOP
β-Actin
CHOP (Fold change)
BiP (Fold change)

Fig. 3

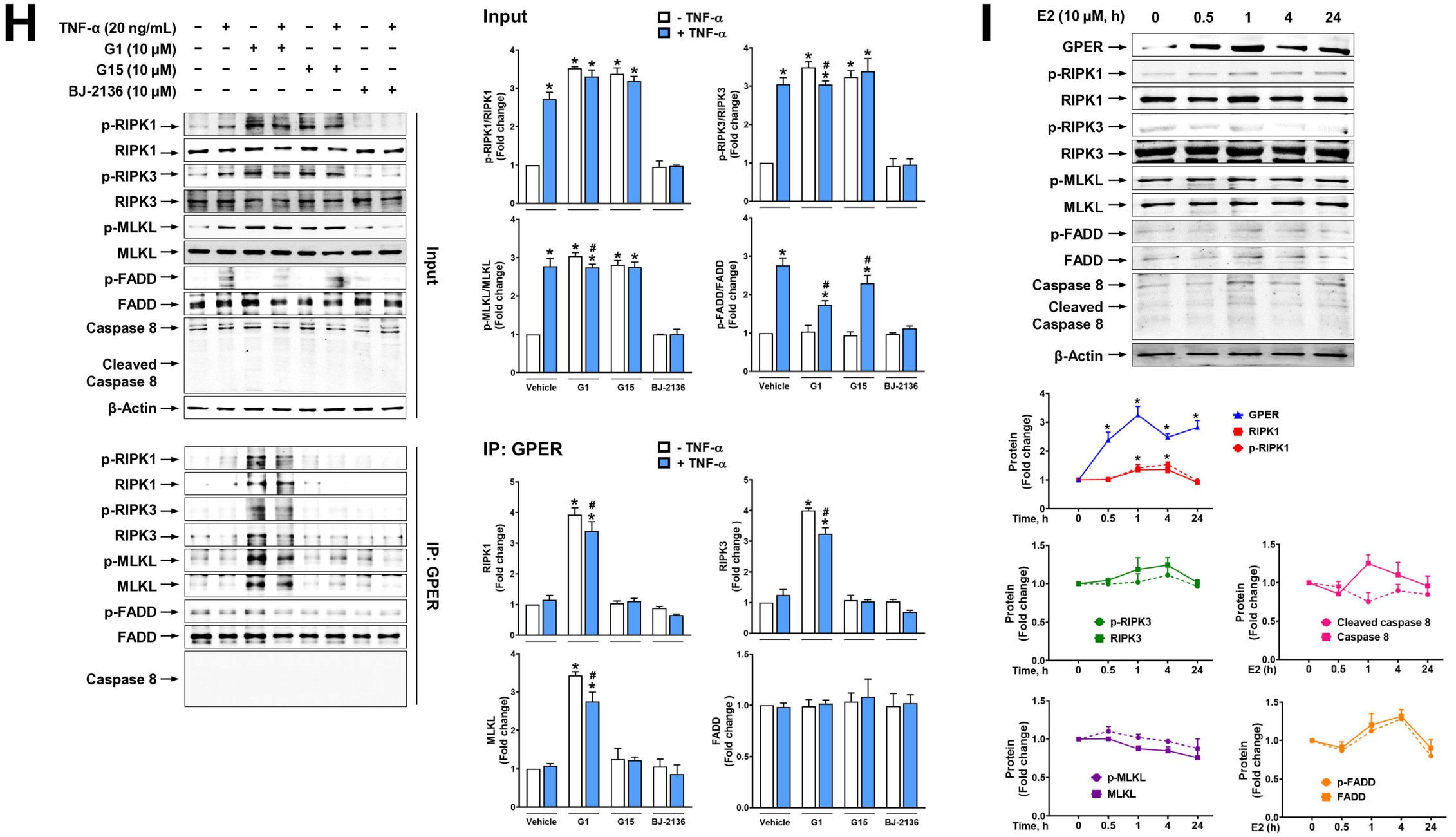
H
TNF-α (20 ng/mL)
G1 (10 μM)
G15 (10 μM)
BJ-2136 (10 μM)
p-RIPK1
RIPK1
p-RIPK3
RIPK3
p-MLKL
MLKL
p-FADD
FADD
Caspase 8
Cleaved Caspase 8
β-Actin
Input
IP: GPER
Input
- TNF-α
+ TNF-α
p-RIPK1/RIPK1 (Fold change)
p-RIPK3/RIPK3 (Fold change)
p-MLKL/MLKL (Fold change)
p-FADD/FADD (Fold change)
Vehicle
G1
G15
BJ-2136
IP: GPER
RIPK1 (Fold change)
RIPK3 (Fold change)
MLKL (Fold change)
FADD (Fold change)
I
E2 (10 μM, h)
0
0.5
1
4
24
Protein (Fold change)
Time, h
GPER
RIPK1
p-RIPK1
p-RIPK3
RIPK3
Cleaved caspase 8
Caspase 8
E2 (h)
p-MLKL
MLKL
p-FADD
FADD

Fig. 4

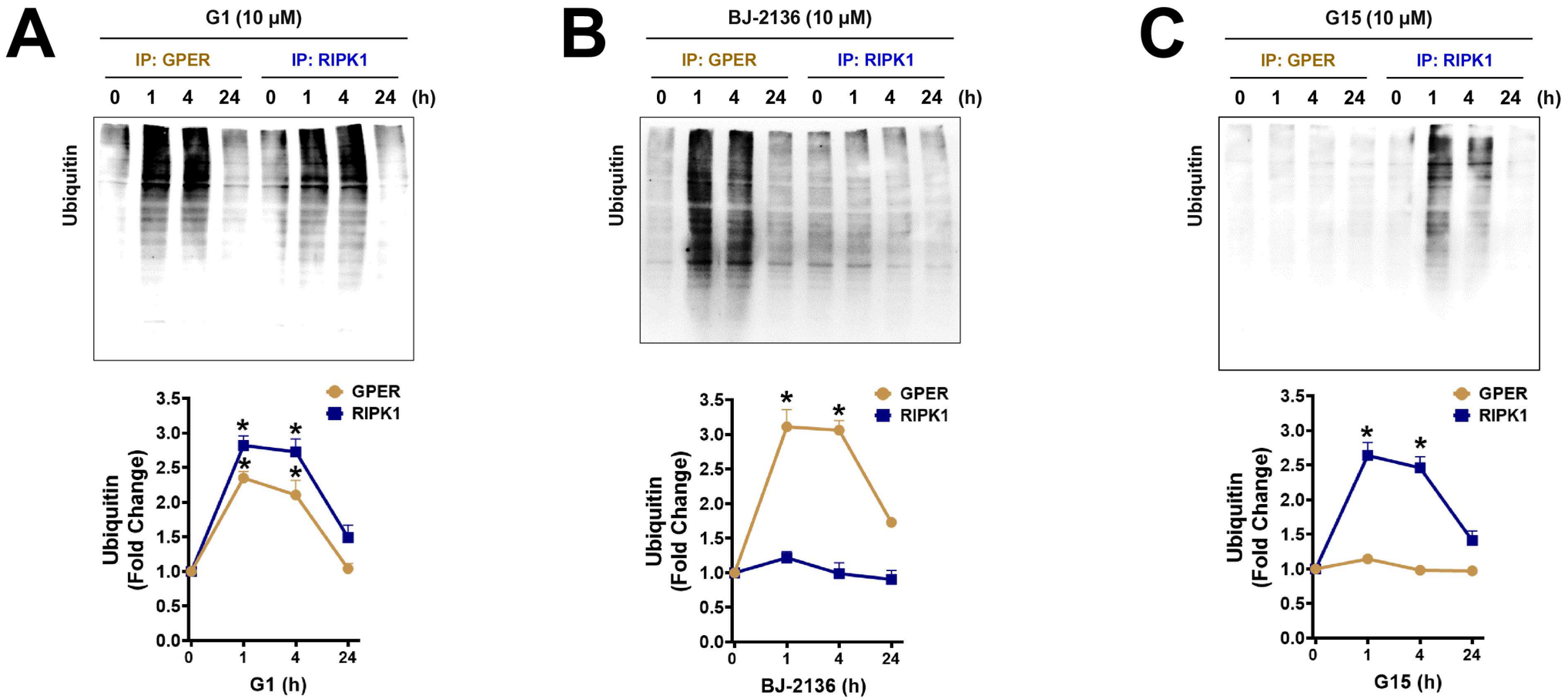
A
G1 (10 μM)
IP: GPER
IP: RIPK1
0 1 4 24 0 1 4 24 (h)
Ubiquitin
GPER
RIPK1
Ubiquitin (Fold Change)
G1 (h)
B
BJ-2136 (10 μM)
IP: GPER
IP: RIPK1
0 1 4 24 0 1 4 24 (h)
Ubiquitin
GPER
RIPK1
Ubiquitin (Fold Change)
BJ-2136 (h)
C
G15 (10 μM)
IP: GPER
IP: RIPK1
0 1 4 24 0 1 4 24 (h)
Ubiquitin
GPER
RIPK1
Ubiquitin (Fold Change)
G15 (h)

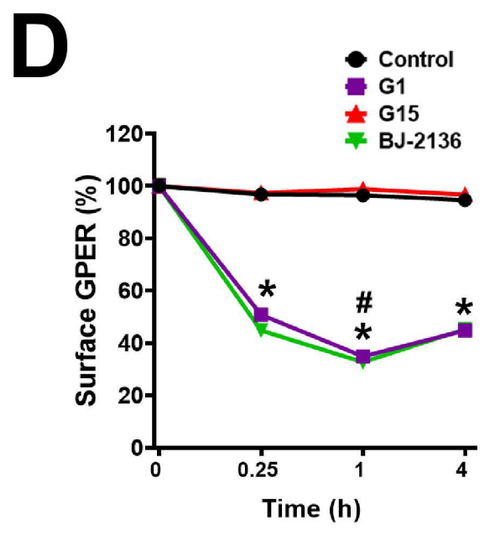
D
Control
G1
G15
BJ-2136
Surface GPER (%)
Time (h)

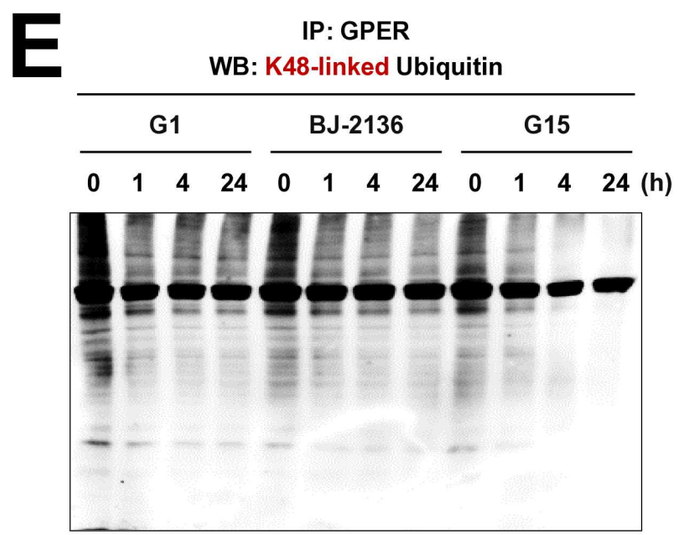
E
IP: GPER
WB: K48-linked Ubiquitin
G1
BJ-2136
G15
0 1 4 24 0 1 4 24 0 1 4 24 (h)

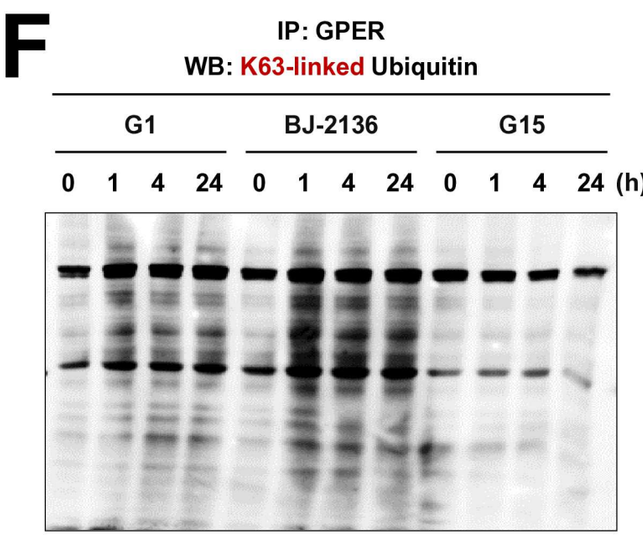
F
IP: GPER
WB: K63-linked Ubiquitin
G1
BJ-2136
G15
0 1 4 24 0 1 4 24 0 1 4 24 (h)

Fig. 5

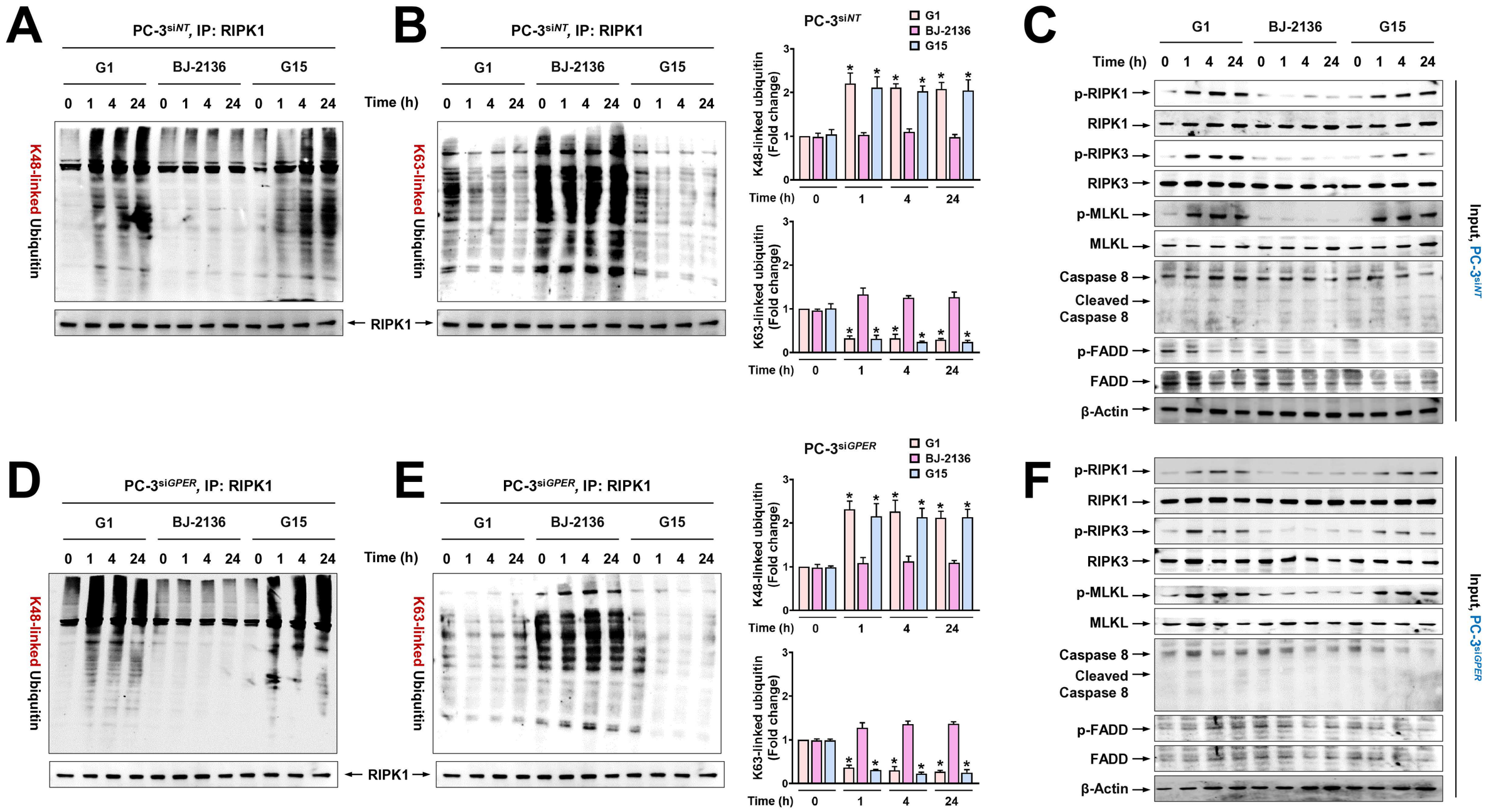
A
PC-3siNT, IP: RIPK1
G1
BJ-2136
G15
0 1 4 24 0 1 4 24 0 1 4 24
K48-linked Ubiquitin
RIPK1
B
PC-3siNT, IP: RIPK1
Time (h)
K63-linked Ubiquitin
PC-3siNT
G1
BJ-2136
G15
K48-linked ubiquitin (Fold change)
K63-linked ubiquitin (Fold change)
C
Time (h) 0 1 4 24 0 1 4 24 0 1 4 24
p-RIPK1
RIPK1
p-RIPK3
RIPK3
p-MLKL
MLKL
Caspase 8
Cleaved Caspase 8
p-FADD
FADD
β-Actin
Input, PC-3siNT
D
PC-3siGPER, IP: RIPK1
E
PC-3siGPER, IP: RIPK1
PC-3siGPER
F
Input, PC-3siGPER

Fig. 5

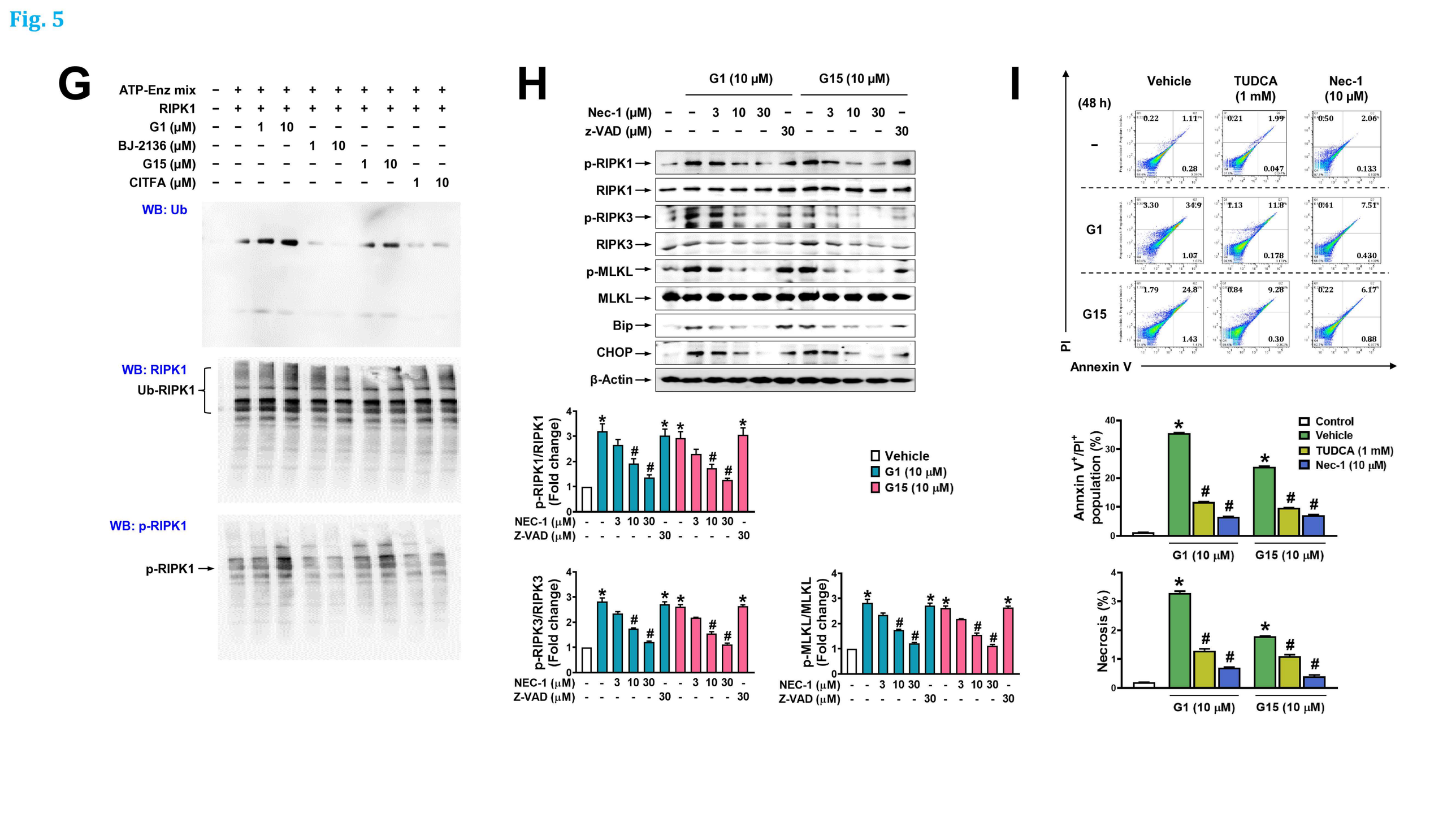
G
ATP-Enz mix
RIPK1
G1 (μM)
BJ-2136 (μM)
G15 (μM)
CITFA (μM)
WB: Ub
WB: RIPK1
Ub-RIPK1
WB: p-RIPK1
p-RIPK1
H
G1 (10 μM)
G15 (10 μM)
Nec-1 (μM)
z-VAD (μM)
p-RIPK1
RIPK1
p-RIPK3
RIPK3
p-MLKL
MLKL
Bip
CHOP
β-Actin
p-RIPK1/RIPK1 (Fold change)
p-RIPK3/RIPK3 (Fold change)
p-MLKL/MLKL (Fold change)
NEC-1 (μM)
Z-VAD (μM)
Vehicle
G1 (10 μM)
G15 (10 μM)
I
Vehicle
TUDCA (1 mM)
Nec-1 (10 μM)
(48 h)
G1
G15
PI
Annexin V
Annexin V+/PI+ population (%)
Control
Vehicle
TUDCA (1 mM)
Nec-1 (10 μM)
Necrosis (%)

Fig. 6

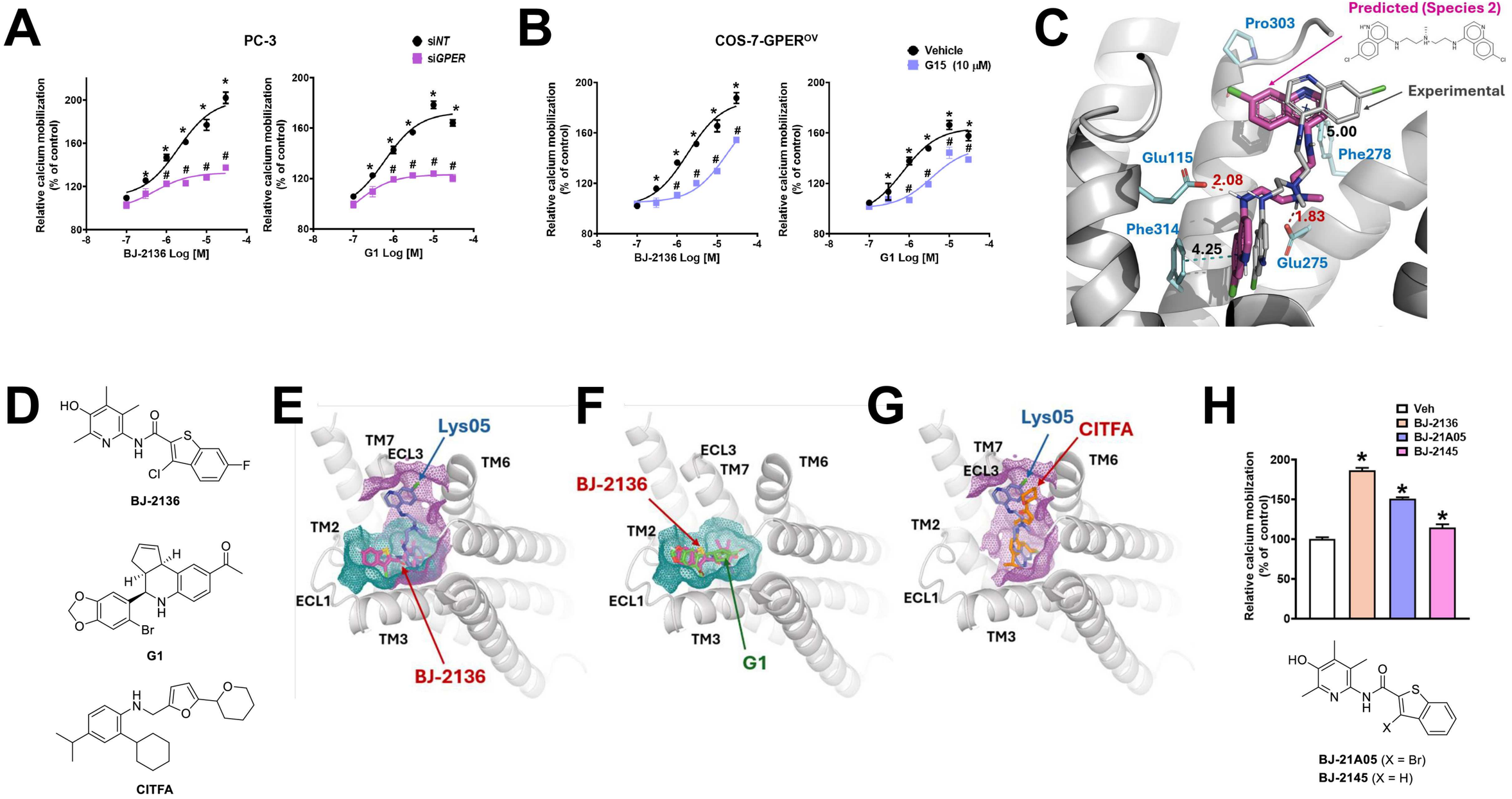
A
PC-3
siNT
siGPER
Relative calcium mobilization (% of control)
BJ-2136 Log [M]
G1 Log [M]
B
COS-7-GPER^OV
Vehicle
G15 (10 μM)
C
Predicted (Species 2)
Experimental
Pro303
Glu115
Phe278
Phe314
Glu275
5.00
2.08
1.83
4.25
D
BJ-2136
G1
CITFA
E
Lys05
TM7
ECL3
TM6
TM2
ECL1
TM3
BJ-2136
F
ECL3
TM7
TM6
BJ-2136
TM2
ECL1
TM3
G1
G
Lys05
CITFA
TM7
ECL3
TM6
TM2
ECL1
TM3
H
Veh
BJ-2136
BJ-21A05
BJ-2145
Relative calcium mobilization (% of control)
BJ-21A05 (X = Br)
BJ-2145 (X = H)

Table 1. Apparent G15 antagonist affinity estimates derived from G1- and BJ-2136-induced calcium responses.

Agonist	EC_{50} (μM)	EC_{50} with G15 (μM)	Dose ratio	Apparent K_B (μM)
G1	1.11 ± 0.50	6.89 ± 1.49	6.21	1.92
BJ-2136	1.51 ± 0.50	17.94 ± 9.72	11.88	0.92

Note: EC_{50} values are presented as mean ± SEM. Dose ratios and apparent K_B values were calculated from the mean EC_{50} values. Apparent K_B values were estimated assuming competitive antagonism by G15 (10 μM); no confidence intervals were available for these derived quantities.

Supplementary Files

This is a list of supplementary files associated with this preprint. Click to download.

- SupplementaryMaterialWBuncropped261111.pptx
- 0SupplementaryFiguresXTables26.11.16.docx